Department of Physics and Astronomy
University of Heidelberg

Bachelor Thesis in Physics
submitted by

Alexander Fabian Impertro

born in Gerolstein (Germany)

2017

Laser system for magneto-optical cooling and trapping of potassium

This Bachelor Thesis has been carried out by Alexander Fabian Impertro at the
Kirchhoff–Institut für Physik
under the supervision of
Prof. Dr. Markus K. Oberthaler

Laser system for magneto-optical cooling and trapping of potassium

This thesis reports on the setup and alignment of an all-diode laser system to cool ^{39}K atoms in a magneto-optical trap (MOT). The laser system is based on two external-cavity diode lasers, which are stabilized to the ^{39}K D1- and D2-transitions by Doppler-free spectroscopy. Our experimental approach uses a 2D-MOT to produce a continuous beam of cold potassium atoms. This allows an efficient loading of the 3D-MOT, where the atoms will be cooled to quantum degeneracy. As the combined 2D-3D-MOT trapping scheme requires a significant amount of optical power, two home-built tapered amplifier modules were set up which provide more than 800 mW of single-mode laser radiation. Combined with optical fibers between every major stage of the laser system, this approach promises a stable and easy-to-maintain everyday operation. The recent observation of a ^{39}K 3D-MOT confirms the correct operation of the laser system.

Lasersystem zum magnetooptischen Kühlen und Fangen von Kalium

Die vorliegende Bachelorarbeit beschreibt den Aufbau und die Justage eines halbleiterbasierten Lasersystems zur Kühlung von ^{39}K Atomen in einer magnetooptischen Falle (MOT). Das Lasersystem basiert auf zwei gitterstabilisierten Diodenlasern, die mithilfe von dopplerfreier Sättigungsspektroskopie auf die D1- und D2-Übergänge in ^{39}K stabilisiert werden. Der experimentelle Aufbau enthält eine 2D-MOT, die einen kontinuierlichen Strahl kalter Kaliumatome erzeugt. Dies erlaubt ein effizientes Laden der 3D-MOT, in der die Atome bis zur Quantenentartung heruntergekühlt werden sollen. Um das kombinierte 2D-3D-MOT Fallenschema mit ausreichend optischer Leistung zu versorgen, wurden zwei Eigenbau-Trapezverstärker-Module aufgebaut, die mehr als 800 mW Licht in einer einzigen räumlichen Mode liefern. Da zusätzlich jeder Teil des Lasersystems durch Lichtleitfasern getrennt ist, verspricht dieser Ansatz einen stabilen und einfach wartbaren Alltagsbetrieb. Die kürzliche Beobachtung einer ^{39}K 3D-MOT bestätigt die korrekte Operation des Lasersystems.

Contents

List of Figures

1 Introduction

During the last century, the hunt for ever lower temperatures has revealed an astonishing amount of new physical phenomena. With the advent of laser cooling, a completely new approach to ultra-low temperature physics was born. Proposed in 1975 by Hänsch and Schawlow [1], experiments using laser cooling were able to create microkelvin samples of dilute atomic clouds. During this time, it was unclear whether the approach towards quantum degeneracy would be preempted by conventional condensation into liquid or solid phases. However, the advance into nanokelvin regimes combined with the use of extremely dilute atomic vapors rewarded the efforts with the first successful demonstrations of a Bose-Einstein condensate (BEC) in 1995 [2, 3].

BECs are extraordinarily powerful quantum systems as they can be manipulated precisely and are by nature extremely pure. Perhaps the most striking property is that although they are macroscopic and thus easily observable, their behavior is completely determined by quantum mechanics. A BEC can be regarded as a matter wave field that is quantized due to the discrete set of atoms forming it. In addition to the interesting intrinsic properties, such as the formation of vortices [4], BECs are especially suited as quantum simulators for quantum systems that are so far not directly observable. A crucial step was the realization of optical lattices which can be used to mimic crystalline systems [5]. When a BEC is held in an optical lattice and the potential depth is increased, the condensate undergoes a quantum phase transition from the superfluid phase to a Mott insulator, in which the atoms are localized to single lattice sites [6, 7]. The observation of Feshbach resonances in an ultracold gas, which allow tuning the interaction strength of the particles via an external magnetic field, was another milestone for the precise manipulation of these quantum systems [8].

The creation of a degenerate quantum gas usually starts with a laser cooling phase followed by forced evaporative cooling. To efficiently initiate evaporation, the atoms need to have a well-resolved energy level structure, allowing for cooling below the Doppler limit, and exhibit a sufficiently high collision rate. These requirements are comparably easy to fulfill for most alkali metals. An especially interesting alkali is potassium, which naturally appears in both fermionic and bosonic isotopes and has broad Feshbach resonances at moderate magnetic fields [9]. However, the most abundant isotope – the bosonic ^{39}K – breaks both requirements. Due to the narrow hyperfine spacing of the excited level, conventional sub-Doppler cooling techniques are very inefficient. Additionally, ^{39}K has a small and negative background scattering length at zero magnetic field, which leads to a minimum of the collision cross section (Ramsauer-

Townsend minimum) [10] which hinders an efficient evaporation. These problems can, for example, be circumvented by using another species such as rubidium to sympathetically cool potassium [11]. However, this significantly complicates the experimental system and sequence. Recently, advanced sub-Doppler cooling techniques like the gray molasses [12, 13] combined with the direct transfer to an optical dipole trap led to Bose-Einstein condensation of ^{39}K [14, 15].

Throughout the course of this thesis, an all-diode laser system for the cooling and trapping of ^{39}K atoms has been constructed. Diode lasers have recently gained much attention in atomic physics because they pose a cost-effective, small and stable alternative to most other sources of coherent radiation. The addition of a gray molasses to the trapping and cooling light requires a system of two lasers which drive the D1- and D2-transitions in ^{39}K. To achieve a high loading rate of a 3D-MOT, an additional 2D-MOT is used as a source of cold atoms. First realized in 1998 by the group of J. Walraven [16], a 2D-MOT compresses atoms through transversal cooling to one axis, along which the atoms can be extracted as a continuous beam. This method poses an compact and effective alternative to the usual approach of a Zeeman slower [17]. Because the two traps require a considerable amount of optical power, two custom tapered amplifier modules were set up which provide the traps with stable and easily adjustable coherent radiation.

Outline of this thesis

This thesis reports on the construction of a laser system for the trapping of ^{39}K atoms in a magneto-optical trap. The main part of this thesis covers the development of the laser system, which is extensively described in Chapter 3. The accompanying theory of laser cooling and trapping is introduced beforehand in Chapter 2. In the following, Chapter 4 reports the strategies to align the optics for 2D- and 3D-MOTs. The alignment was done using Rb atoms because a well-adjusted laser system from a previous experiment was available, which led to a quick observation of a Rb 3D-MOT. The thesis is concluded with the successful switch to ^{39}K atoms and the observation of a 3D-MOT as well as an outlook on the future of the experiment.

2 Laser Cooling and Trapping

Laser cooling and trapping of atoms has proven to be the basis of many exciting experiments in modern atomic physics. The idea was initially proposed by Wineland and Dehmelt [18] and independently by Hänsch and Schawlow [1] in 1975. A series of experiments at NIST [19, 20] and the Bell Labs [21] soon realized the proposals, opening up a whole new subfield. The early developments culminated in the first observations of a previously unseen phase transition, the Bose-Einstein condensation, by the groups of Cornell/Wieman [22] and Ketterle [2, 3] in 1995. Nowadays, state of the art experiments routinely cool down atoms by more than nine orders of magnitude on the temperature scale. This section will summarize the theoretical basics of laser cooling [23–25] which are necessary to understand the working principles of the employed techniques.

2.1 Light Forces

To cool and trap atoms, their interaction with optical fields plays the key role. During the interaction, several conservation laws have to be fulfilled. Energy conservation results in a resonance condition for the frequency of the optical field, while angular momentum conservation leads to a selection rule for the atom's orbital angular momentum l. Additionally, linear momentum conservation causes a change of the atom's motion in the laboratory frame. The momentum transfer corresponds to a force which is the basis of laser cooling.

An intuitive understanding of the origin and working mechanisms of these light forces can be gained by analyzing a two-level atom in a light field that propagates in z-direction. The following derivation is based on [23].

The two-level system

A two-level atom with a ground state $|g\rangle$ and an excited state $|e\rangle$ (Fig. 2.1) is described by the unperturbed, time-independent atomic Hamiltonian $\mathcal{H}_0$. Both states are eigenstates of $\mathcal{H}_0$ with an energy $\hbar\omega_{\mathrm{g,e}}$ such that

$$\mathcal{H}_0 |g\rangle = \hbar\omega_{\mathrm{g}} |g\rangle , \mathcal{H}_0 |e\rangle = \hbar\omega_{\mathrm{e}} |e\rangle . \tag{2.1}$$

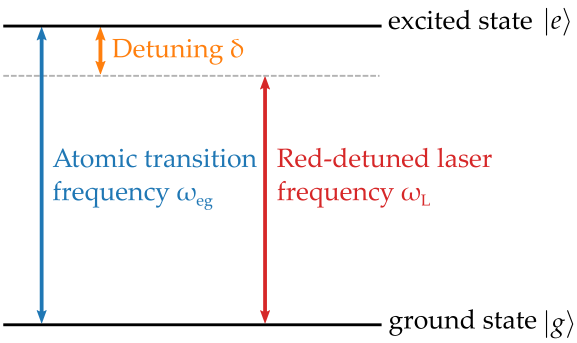

Figure 2.1: Two-level system. Energy diagram for a two-level system with ground state $|g\rangle$ and excited state $|e\rangle$. The detuning δ is the difference of the atomic resonance frequency ω_{eg} from the laser frequency ω_{L}.

The addition of a monochromatic light field perturbs the atom, and the total system can be described by the combined atom-light Hamiltonian

$$\mathcal{H}(t) = \mathcal{H}_0 + \mathcal{H}'(t), \tag{2.2}$$

where the light field $\vec{\mathcal{E}}(\vec{r}, t) = \mathcal{E}_0 \hat{e} \cos(kz - \omega_L t)$ induces the perturbation

$$\mathcal{H}'(t) = -e\vec{\mathcal{E}}(\vec{r}, t) \cdot \vec{r}. \tag{2.3}$$

At any given time t, the atom is expected to be in a superposition of the eigenstates:

$$|\psi(t)\rangle = c_{\mathrm{g}}(t) e^{-i\omega_{\mathrm{g}} t} |g\rangle + c_{\mathrm{e}}(t) e^{-i\omega_{\mathrm{e}} t} |e\rangle \,. \tag{2.4}$$

The state amplitudes $c_{\mathrm{g,e}}(t)$ can be determined by solving the time-dependent Schrödinger equation. Under rotating wave and dipole approximations [24], this ansatz yields a set of two uncoupled differential equations:

$$\begin{cases} \ddot{c}_{\mathrm{g}}(t) - i\delta \dot{c}_{\mathrm{g}}(t) + \dfrac{\Omega^2}{4} c_{\mathrm{g}}(t) = 0, \\ \ddot{c}_{\mathrm{e}}(t) + i\delta \dot{c}_{\mathrm{e}}(t) + \dfrac{\Omega^2}{4} c_{\mathrm{e}}(t) = 0. \end{cases} \tag{2.5}$$

Here, $\Omega = \frac{-eE_0}{\hbar} \langle e|r|g\rangle$ is the Rabi frequency and $\delta = \omega_{\mathrm{L}} - \omega_{\mathrm{eg}}$ is the laser detuning from the atomic resonance. Ω is assumed to be a positive, real number. The solutions for c_{g} and c_{e} show oscillatory behavior, which also leads to an oscillating probability to find the atom in the ground or excited state (given by $|c_{\mathrm{g}}|^2$ and $|c_{\mathrm{e}}|^2$). The frequency of this oscillation is called generalized Rabi frequency and is given by $\Omega' = \sqrt{\Omega^2 + \delta^2}$.

Until now, only transitions stimulated by the light field have been included into the treatment. Due to the finite excited state lifetime, the atom can undergo a spontaneous decay, emitting a photon into a random direction. As long as the emitted photon remains unobserved, the system is no longer in a pure state but in a statistical mixture, which requires a description using the density matrix formalism.

For a two-level system in a pure state, the density matrix can be written as

$$\rho = \begin{pmatrix} \rho_{\mathrm{ee}} & \rho_{\mathrm{eg}} \\ \rho_{\mathrm{ge}} & \rho_{\mathrm{gg}} \end{pmatrix} = \begin{pmatrix} |c_{\mathrm{e}}|^2 & c_{\mathrm{e}}c_{\mathrm{g}}^* \\ c_{\mathrm{g}}c_{\mathrm{e}}^* & |c_{\mathrm{g}}|^2 \end{pmatrix}. \tag{2.6}$$

The spontaneous decay results in an exponential decay of the coefficient $\rho_{\mathrm{eg}}(t)$ with a constant rate $\gamma/2$, where γ^{-1} is the excited state lifetime. The four independent parameters of ρ can be reduced to only two by exploiting $\rho_{\mathrm{gg}} + \rho_{\mathrm{ee}} = 1$ (conservation of population) and $\rho_{\mathrm{eg}} = \rho_{\mathrm{ge}}^*$. Introducing the population difference $w := \rho_{\mathrm{gg}} - \rho_{\mathrm{ee}}$, the following set of equations is obtained:

$$\begin{cases} \dot{\rho}_{\mathrm{eg}}(t) = -\left(\frac{\gamma}{2} - i\delta\right)\rho_{\mathrm{eg}}(t) + \frac{1}{2}iw\Omega \\ \dot{w}(t) = -\gamma w + \gamma - i\left(\Omega\rho_{\mathrm{eg}}^* - \Omega^*\rho_{\mathrm{eg}}\right) \end{cases} \tag{2.7}$$

These equations are called the *Optical Bloch Equations* and fully describe the dynamics of a two-level system. An equilibrium state implies vanishing time derivatives, which leads to

$$\begin{cases} w = \dfrac{\delta^2 + \gamma^2/4}{\delta^2 + \Omega^2/2 + \gamma^2/4} \\ \rho_{\mathrm{eg}} = \dfrac{i\Omega(\gamma + 2i\delta)}{4\delta^2 + 2\Omega^2 + \gamma^2} \end{cases}. \tag{2.8}$$

Since the Rabi frequency scales with light intensity ($\Omega^2 \propto I$), the system's response to an applied light field is highly intensity-dependent. This dependence can be quantified in terms of the *saturation parameter*

$$s_0 := \frac{2\Omega^2}{\gamma^2} = \frac{I}{I_{\mathrm{s}}}. \tag{2.9}$$

It describes the ratio of the applied intensity I to the *saturation intensity*

$$I_{\mathrm{s}} := \frac{\pi\gamma hc}{3\lambda^3}, \tag{2.10}$$

at which the transition starts to saturate. Here, λ is the transition wavelength and γ the lifetime of the excited state. The saturation effect can be seen by regarding the equilibrium excited state population ρ_{ee} given by

$$\rho_{\mathrm{ee}} = \frac{1}{2}(1 - w) = \frac{s_0/2}{1 + s_0 + (2\delta/\gamma)^2}. \tag{2.11}$$

For high intensities ($s_0 \gg 1$), ρ_{ee} approaches $1/2$, which means that no more than half of the ground state population can be excited. In steady state, the total scattering rate γ_{sc} of light from the laser field is given by

$$\gamma_{\mathrm{sc}} = \gamma\rho_{\mathrm{ee}} = \left(\frac{s_0}{1+s_0}\right)\left(\frac{\gamma/2}{1+\left[2\delta/\left(\gamma\sqrt{1+s_0}\right)\right]^2}\right), \tag{2.12}$$

because the excitation rate exactly balances the decay rate γ. For high intensities, the scattering rate γ_{sc} saturates to $\gamma/2$. Due to this saturation, atomic transitions as observed in an experiment appear broadened from their natural linewidth γ to

$$\gamma' = \gamma\sqrt{1+s_0}. \tag{2.13}$$

This effect is called *power broadening*, and has to be considered especially for spectroscopic experiments, where the saturation parameter s_0 must be kept as low as possible in order to observe narrow lines.

Force on an atom at rest

In each absorption process, the light field with wavenumber $\vec{k}$ transfers a momentum $\hbar\vec{k}$ to the atom. A following spontaneous emission causes a recoil in a random direction. Over many such absorption-emission cycles, the momentum transfer due to spontaneous emission averages to zero. Consequently, the net momentum is determined only by the absorption. Because an atom has to relax before it can absorb a new photon, the repetition rate for this process is determined by the spontaneous emission rate γ_p, which leads to the force

$$F_{\mathrm{sc}} = \hbar\vec{k}\gamma\rho_{\mathrm{ee}} = \frac{\hbar\vec{k}s_0\gamma/2}{1+s_0+(2\delta/\gamma)^2}. \tag{2.14}$$

This *scattering force* is of dissipative nature and saturates for high intensities to $F_{\max} = \hbar\vec{k}\gamma/2$.

2.2 Laser Cooling and Optical Molasses

By carefully choosing geometry and light frequency, atoms can be cooled by exploiting the Doppler effect. Due to the Doppler shift, the resonance frequency and hence the momentum exchange becomes velocity-dependent. This velocity dependence is the reason why radiative forces can be used to decelerate and cool atoms. The scattering force, as derived in Eq. 2.14 for an atom at rest, can easily be adapted to the case of an atom in motion. An atom with finite velocity v sees the light Doppler-shifted from its value in the laboratory system. If this shift is small compared to the laser detuning δ, it can be accounted for by the replacement $\delta \to \delta + \omega_{\mathrm{D}}$. The force on a moving atom is thus given by

$$\vec{F}_{\mathrm{sc}} = \frac{\hbar\vec{k}s_0\gamma/2}{1+s_0+(2(\delta+\omega_{\mathrm{D}})/\gamma)^2}, \tag{2.15}$$

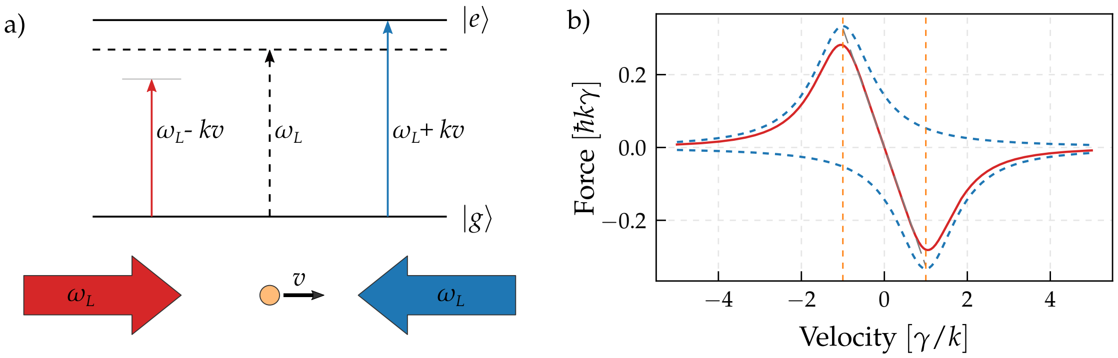

Figure 2.2: 1-D Optical molasses. a) Energy scheme for a two-level atom subject to a 1-D optical molasses. The laser beams are red-detuned, and the opposing beam is Doppler-shifted into resonance . b) Velocity dependence of the optical damping forces. The dashed traces show the force from each beam, while the solid curve is their sum. Between the maxima at v_c, the net force is approximately linear (and thus purely viscous). Calculated for $s_0 = 2$ and $\delta = -\gamma$.

where $\omega_\mathrm{D} = -\vec{k} \cdot \vec{v}$ is the Doppler shift seen by the moving atoms. The sign is chosen such that a $\vec{k}$ anti-parallel to $\vec{v}$ produces a positive (blue) shift.

Optical molasses

In one dimension, a sample of atoms with a finite (thermal) velocity v can be cooled by placing it in the overlap region of two counter-propagating lasers of equal frequency, intensity and polarization. Atoms moving towards one of the beams experience a net force given by $\vec{F}_\mathrm{OM} = \vec{F}_+ + \vec{F}_-$, where

$$\vec{F}_\pm = \pm \frac{\hbar \vec{k} \gamma}{2} \frac{s_0}{1 + s_0 + \left[2\left(\delta \mp |\omega_\mathrm{D}|\right)/\gamma\right]^2}. \tag{2.16}$$

The effects of the individual lasers can be intuitively understood by looking at the energy diagram of the transition. For red-detuned light ($\delta < 0$), the situation is shown in Fig. 2.2a. If the atom moves to the right, the laser beam coming from the right side is blue-shifted into resonance in the atom's reference frame, whereas the beam coming from the left is red-shifted further out of resonance. Hence, the atom mostly scatters light from the counter-propagating beam and is effectively slowed. If the atom moves to the left, the situation is reversed: The left beam is now in resonance and again, the atom is slowed. In this setup, the atom's velocity component parallel to the red-detuned laser beams is decreased independently of its direction.

The force from the individual beams as well as the sum force is shown in Fig. 2.2b as a function of the atom's velocity. $\vec{F}_\mathrm{OM}$ has two clear maxima located at

$$v_\pm = \pm \frac{\gamma'}{2k\sqrt{3}} \sqrt{\left(\frac{2\delta}{\gamma'}\right)^2 - 1 + 2\sqrt{\left(\frac{2\delta}{\gamma'}\right)^4 + \left(\frac{2\delta}{\gamma'}\right)^2 + 1}}. \tag{2.17}$$

For the usual range of parameters (e.g. $s_0 \leq 1$ and $\delta = -\gamma/2$), the location of the extremal points can be approximated by

$$v_c = \gamma/k. \tag{2.18}$$

Between these points, the slowing force is approximately proportional to the velocity of the atoms:

$$\vec{F}_{\mathrm{OM}} \approx \frac{8\hbar k^2 \delta s_0 \vec{v}}{\gamma \left(1 + s_0 + (2\delta/\gamma)^2\right)^2} \equiv -\beta \vec{v}. \tag{2.19}$$

For $\delta < 0$, it opposes the velocity and viscously damps the atomic motion, giving this technique the name *optical molasses*. Because the force causes pure viscous damping for atoms slower than the velocity given by Eq. 2.18, this velocity range is also called the *capture range*. For a ^{39}K atom on the D2-line, the capture velocity is $v_c = 4.63\,\mathrm{m/s}$. Comparing this to the mean thermal velocity of potassium atoms at 70 °C $v_{\mathrm{th}} = \sqrt{\frac{2k_BT}{M}} \approx 382.5\,\mathrm{m/s}$, it is clear that optical molasses is only able to capture the very low tail of the velocity distribution.

Eq. 2.19 implies the unphysical limit of a deceleration towards $v = 0$. This occurs because heating processes caused by spontaneous emission were neglected. The average momentum transfer of many spontaneous emission events is zero, but the rms scatter is finite. Hence, the atom is subject to a heating rate that becomes important especially at low temperatures. The competition between this heating and the Doppler cooling results in a steady state with a kinetic energy of

$$E_{\mathrm{stead}} = \left(\frac{\hbar\gamma}{8}\right)\left(\frac{2|\delta|}{\gamma} + \frac{\gamma}{2|\delta|}\right). \tag{2.20}$$

The steady state energy is minimal for $\delta = -\gamma/2$, corresponding to a temperature of

$$T_D = \frac{\hbar\gamma}{2k_B}. \tag{2.21}$$

This temperature is called the *Doppler temperature*, and is the theoretical limit for Doppler cooling in a two-level atom. For ^{39}K on the D2-line, the Doppler limit occurs at a temperature of $T_D = 145\,\mu\mathrm{K}$.

The principle of optical molasses can be extended by using three intersecting orthogonal pairs of counter-propagating beams, which results in a restriction of the atomic motion in all three dimensions. Many atoms can thereby be collected and cooled in a small volume. While the detainment times can be remarkably long (several seconds for a beam waist of 1 cm), an optical molasses is not a trap for neutral atoms because of the missing restoring force. To achieve trapping, an additional magnetic field can be employed.

2.3 The Magneto-Optical Trap

The magneto-optical trap (MOT) as a hybrid employing both optical and magnetic fields is the most widely used trap for neutral atoms. In addition to the restriction in momentum

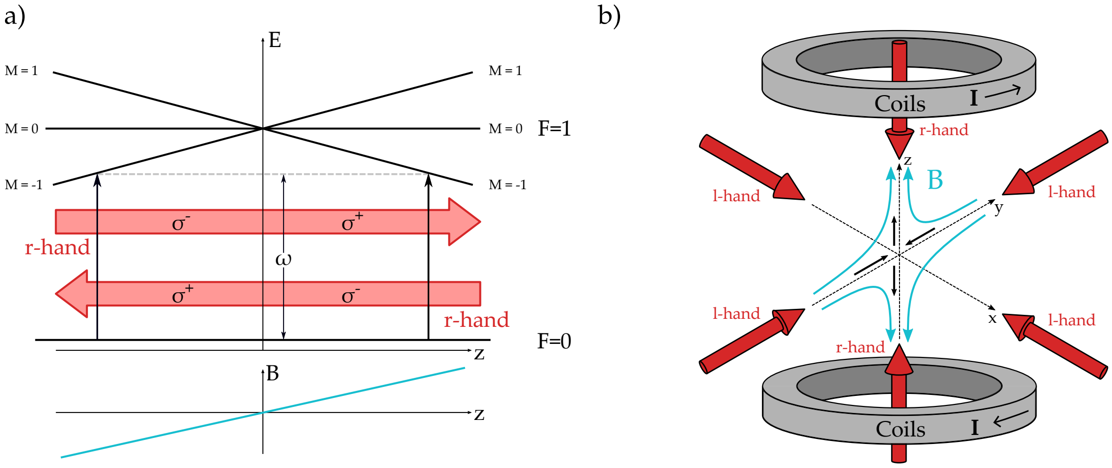

Figure 2.3: Magneto-optical trap. a) Energy diagram for a $|F=0\rangle \rightarrow |F=1\rangle$ transition. The quadrupole field causes a spatially dependent Zeeman shift. With red-detuned circularly polarized lasers, the atom scatters photons from the beam which points towards the trap center. This creates a restoring force, confining the atom at $z=0$. b) Schematic drawing of a magneto-optical trap (MOT). The quadrupole field is created by two coils in anti-Helmholtz configuration, six orthogonal molasses beams cause a 3-D confinement. Note that because of the specific field shape, the vertical beams have the opposite handedness of the horizontal beams. Figure based on [24].

space from the optical molasses, inhomogeneous magnetic fields allow an absolute spatial confinement. The principle of a MOT is illustrated in Fig. 2.3 for a simple $|F=0\rangle \rightarrow |F=1\rangle$ transition in 1-D. The counter-propagating laser beams are circularly polarized with equal handedness and red-detuned to the atomic resonance. In addition, quadrupole coils produce a homogeneous field gradient around $B=0$ in the center of the coil arrangement. Due to the Zeeman effect, the magnetic sub-levels of the excited state are no longer degenerate and shift linearly with the position of the atom. For the following description, the quantization axis is locally chosen to coincide with the direction of the magnetic field. If an atom has a positive displacement ($z>0$), the $|1,-1\rangle$ state is closest to resonance with the laser light. With respect to the choice of the quantization axis, the beam coming from the right drives σ^--transitions, whereas the beam coming from the left drives σ^+-transitions. Hence, the selection rules for electric dipole transitions demand that photons are scattered from the beam coming from the right, which leads to a scattering force pushing the atom back to the trap center. A similar situation arises for negative displacements ($z<0$), in which photons are scattered from the beam coming from the left. This spatial confinement acts simultaneously with the viscous damping from the optical molasses, making the MOT a particularly effective tool to trap and cool atoms.

Mathematically, the effect of the magnetic field can be treated as an additional detuning. The total detuning is thus the sum of the laser detuning, the velocity-dependent Doppler shift and the field-dependent Zeeman shift and can be written as

$$\delta_{\pm} = \delta \mp \vec{k} \cdot \vec{v} \pm \mu' B/\hbar. \tag{2.22}$$

The Zeeman shift depends on the effective magnetic moment $\mu' \equiv \left(g_\mathrm{e} M_\mathrm{e} - g_\mathrm{g} M_\mathrm{g}\right) \mu_B$, where the $g_{\mathrm{g/e}}$ are the Landé-factors and the $M_{\mathrm{g/e}}$ are the magnetic quantum numbers for ground and excited state, respectively. Similarly to Eq. 2.16, the force on the atoms can be written as the sum $\vec{F}_\mathrm{MOT} = \vec{F}_+ + \vec{F}_-$ of the individual forces

$$\vec{F}_\pm = \pm \frac{\hbar k \gamma}{2} \frac{s_0}{1 + s_0 + \left(2\delta_\pm/\gamma\right)^2}, \tag{2.23}$$

If the total detuning $\delta_\pm$ is dominated by the laser detuning δ, the resulting force can again be approximated for small velocities and radii, yielding the relation

$$\vec{F}_\mathrm{MOT} \approx -\beta \vec{v} - \kappa \vec{r}, \tag{2.24}$$

where the damping coefficient β is defined in Eq. 2.19, and the spring constant κ is given by $\kappa = \frac{\mu' A}{\hbar k}\beta$, where A denotes the magnetic field gradient. The Zeeman effect causes an imbalance in the radiation pressure forces, which in turn leads to a restoring force. This spatially dependent force pushes the atoms to the trap center and causes an overdamped oscillatory motion.

In contrast to the capture velocity for optical molasses (cf. Eq. 2.18), a MOT has a much larger capture velocity on the order of $v_\mathrm{c} \sim 100\,\mathrm{m/s}$. This is due to the Zeeman shift which is able to compensate the changing Doppler shift over an extended range as the atoms move in the inhomogeneous magnetic field.

2.4 Cooling below the Doppler Limit

Not long after the first experiments with optical molasses had been carried out, several groups measured temperatures significantly below the theoretical Doppler limit [26]. It became clear that the two-level atom picture which had been used to derive the Doppler theory does not include the peculiarities of real multilevel atoms with many hyperfine sub-states. In 1989, Jean Dalibard and Claude Cohen-Tannoudji managed to explain this phenomenon in their theory of Sisyphus cooling [27]. The key to the much lower limit is the occurrence of polarization gradients due to the polarized laser beams and optical pumping between the different hyperfine states.

The mechanism can be understood by analyzing an atom moving through a standing wave that is created by two counter-propagating laser beams with orthogonal linear polarizations, red-detuned with respect to a $|F\rangle \to |F+1\rangle$ transition. A polarization gradient is established, in which the polarization oscillates between right-hand circular to left-hand circular over the course of $\Delta z = \lambda/4$. This leads to a periodic modulation of the light shift for the ground state magnetic sub-levels as can be seen in Fig. 2.4a. If the atom is in a region of right-hand circular polarization, the $M = 1/2$ state is shifted lower than the $M = -1/2$ state. It can be shown that the coupling of the potential hill to the excited state manifold is higher than the

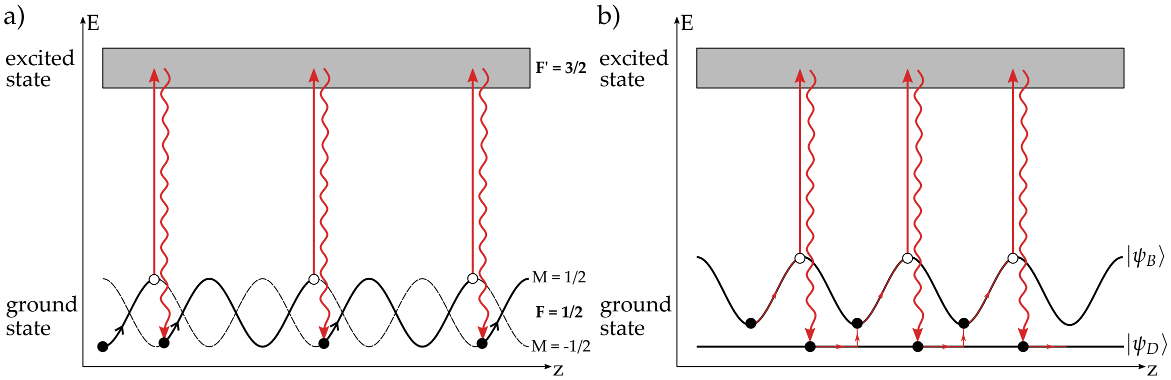

Figure 2.4: Comparison of bright and gray molasses. a) In a bright molasses, the atom is subject to a standing wave with spatially varying polarization, and the AC-Stark shift modulates the energy of the magnetic sublevels. By the right choice of light polarization, the process of an absorption in an intensity maximum and the progressive de-excitation into an intensity minimum is more likely than the opposite process, leading to a strong dissipation force. b) In a gray molasses, atoms can be transferred from a dark to a bright state by motional coupling. In the bright state, the cooling process is equal to bright molasses. Cooled atoms are collected in the dark states, leading to temperatures below the Doppler limit.

coupling of the potential valley. If the atom is excited and subsequently decays to the same state, its kinetic energy does not change. If it decays to the potential valley however, its kinetic energy is decreased on the order of the ground state light shift. The same applies for regions of left-hand circular polarization, and this imbalance in excitation probabilities leads to a strong cooling.

The cooling process is limited by the recoil induced through the spontaneous emission process, hence, the single-photon recoil energy sets a lower bound on the achievable temperatures. Experimentally observed values usually lie one magnitude higher than the *recoil temperature*

$$k_B T_r = \frac{(\hbar k)^2}{2M}, \tag{2.25}$$

where M is the atomic mass. Sisyphus cooling can be inefficient for some elements due to their tight level structure. Recently, some alternative cooling mechanisms have been developed which can enhance the cooling efficiency and lead to even lower temperatures. One of these techniques is the gray molasses, which will be used in this experiment and is shortly introduced in the next section.

Gray molasses

A gray molasses is a cooling technique which can be performed with blue-detuned light with respect to a $F \rightarrow F' = F$ or a $F \rightarrow F' = F - 1$ transition [28, 29]. The light field couples atomic states, which leads to a dressing of the ground state manifold into bright (i.e. coupled to the excited state) states $|\psi_B\rangle$ and dark (i.e. uncoupled) states $|\psi_D\rangle$. It can be shown that bright states experience a positive light shift in the blue-detuned field, whereas dark states remain unshifted. Fig. 2.4b shows an atom that is initially in a bright state and propagates with velocity v along the z-axis. In the bright state, the atom undergoes the normal Sisyphus dissipation process, from where it can decay to either of the states. If it falls back to the bright state, the process repeats. In contrast to that, a decay to the dark state leads to a temporary trapping of the atom. The atom-light interaction Hamiltonian by itself predicts that bright and dark states do not couple, which would imply no transfer processes between the levels. However, the atomic motion requires that the kinetic energy is included into the picture, which leads to a *motional coupling* of bright and dark states. The transfer probability is proportional to the velocity of the atom and inversely proportional to the light shift of the bright state with respect to the dark state. Hence, atoms are most likely to jump into the bright state at a potential minimum which leads to an efficient Sisyphus cooling cycle. Any atom with nonzero velocity will take part in the cooling cycle until it reaches zero velocity and the transition probability vanishes. Resting atoms will accumulate in the dark state, a process known as *velocity-selective coherent population trapping* (VSCPT) [30].

To date, gray molasses is well-established for achieving sub-Doppler temperatures especially in ^{6,7}Li [31–33], but it has also been demonstrated for ^{39}K [12–14].

3 Experimental Setup

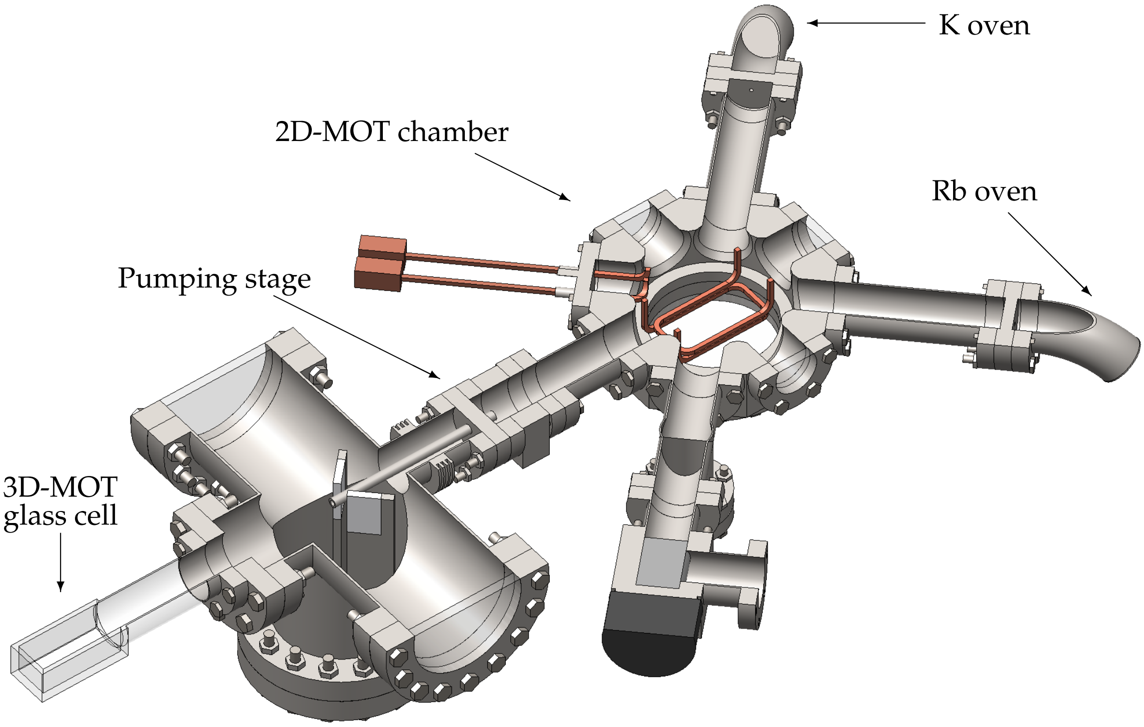

Figure 3.1: Schematic drawing of the vacuum chamber. The vacuum apparatus is split into a 3D-MOT chamber (under Ultra High-Vacuum conditions) and a 2D-MOT chamber (under High-Vacuum conditions), which are isolated by a differential pumping stage. The 2D-MOT chamber is directly connected to separate potassium and rubidium ovens. From [34].

Experiments trapping and manipulating ultracold atoms require extreme vacuum conditions to minimize scattering processes of the cold sample with background gas atoms. The 3D-MOT chamber, realized as a rectangular glass cell for maximum optical access, is therefore operated in a vacuum pressure of better than 10^{-11} mbar. In such an environment, the low partial pressure of the selected atomic species would make a direct loading of the MOT from the background impossible. A popular approach to load a MOT with a high flux is to use a Zeeman slower. However, a Zeeman slower is complicated to build and provides only longitudinal cooling. An elegant method employs a second magneto-optical trap, which is operated in a vacuum chamber with a higher pressure (up to 10^{-8} mbar) and can be loaded directly from the background. Under continuous pumping from both sides, the two chambers can be operated in direct contact by using a *differential pumping stage*. The essential component of a differential pumping stage is a thin and long tube which connects the vacuum chambers. Due to the large mean free path of atoms in these pressure ranges, the conductance of this tube is small enough to allow for a pressure difference of several orders of magnitude between the two ends. The second trap is a *2D-MOT*, in which the cooling and trapping forces act only in two dimensions. This creates a cold atom beam, which allows an efficient loading of the 3D-MOT.

The 2D-MOT consists of two orthogonal pairs of counter-propagating laser beams and elongated coils creating a transversal quadrupole. In this setup, the atoms are cooled in the plane transversally to the differential pumping tube. This leads to the creation of a cigar-shaped atomic cloud, which is still hot in the direction parallel to the tube. When the 2D-MOT is properly aligned with the tube, the atoms can advance into the 3D-MOT chamber, making this approach equivalent to a radially cooled atomic beam. The flux can be additionally enhanced by using a push beam that is aligned with the tube and accelerates the atoms in the direction of the 3D-MOT.

In our experimental setup, the vacuum apparatus originates from a previous KRb double-species experiment and is therefore equipped with separate K and Rb ovens. In the following chapter, some peculiarities of potassium atoms will be presented, which highly influence the requirements for the specific components of laser and vacuum setup.

3.1 Cooling Potassium Atoms

Potassium appears naturally in the form of three isotopes: the bosonic species ^{39}K (natural abundance 93.26 %) and ^{41}K (natural abundance 6.73 %), as well as the fermionic species ^{40}K (natural abundance 0.01 %). The experiment is designed for the bosonic ^{39}K isotope, since it has the highest natural abundance and does not require enriched samples. The strongest visible lines of this isotope are the D1 ($4^2S_{1/2} \rightarrow 4^2P_{1/2}$) and D2 ($4^2S_{1/2} \rightarrow 4^2P_{3/2}$) transitions. The D1 transition has a lifetime of $\tau = 26.72\,\mathrm{ns}$, corresponding to a linewidth of $\gamma = 2\pi \times 5.956\,\mathrm{MHz}$. According to Eq. 2.10, the saturation intensity can be calculated as $I_{\mathrm{sat}} = 1.73\,\mathrm{mW/cm^2}$. Correspondingly, the D2 transition has $\tau = 26.37\,\mathrm{ns}$, $\gamma = 2\pi \times 6.035\,\mathrm{MHz}$ and $I_{\mathrm{sat}} = 1.75\,\mathrm{mW/cm^2}$ [35].

Typically, for cooling and trapping of alkali atoms, two different light frequencies are required. The *cooling* light is tuned to a closed transition and exerts most of the force required for the molasses and trapping mechanisms. Because real atoms usually have more than two levels, off-resonant excitations lead to atoms being optically pumped into a hyperfine ground state that is dark for the cooling laser. The atoms can thus escape the cooling cycle. The *repumping* light is tuned to counteract this process and pump the atoms back into the cooling

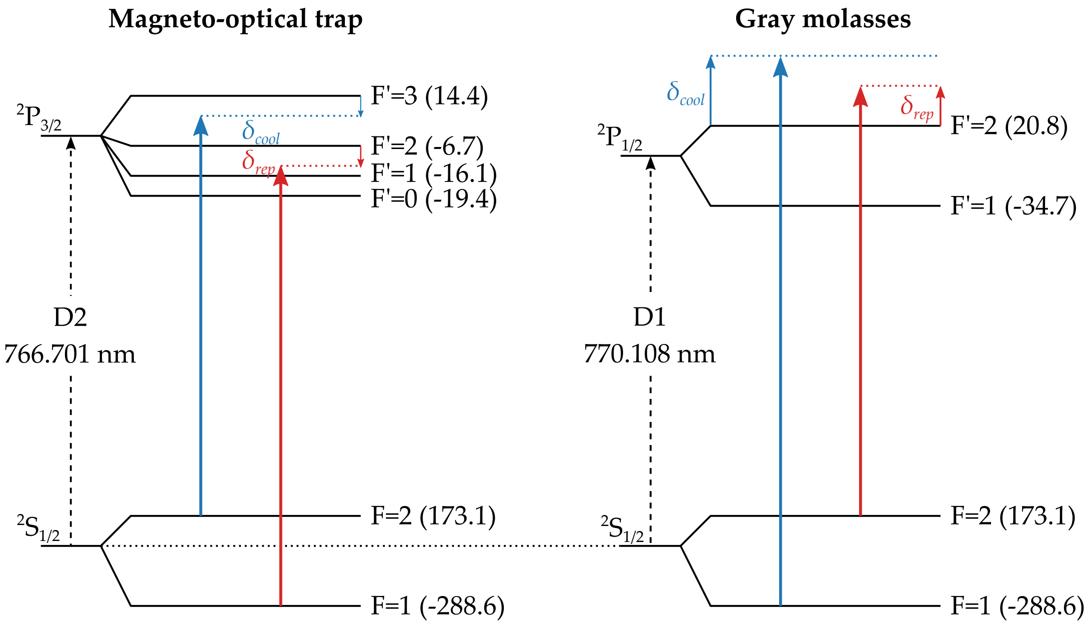

Figure 3.2: Level Structure of the ^{39}K D1- and D2-lines. The magneto-optical trap is driven by two transitions on the D2-line, a cooler red-detuned by δ_{cool} from $|F=2\rangle \rightarrow |F'=3\rangle$, and a repumper red-detuned by δ_{rep} from $|F=1\rangle \rightarrow |F'=2\rangle$. The gray molasses uses a cooling transition ($|F=1\rangle \rightarrow |F'=2\rangle$, blue-detuned by δ_{cool}) and a repumping transition ($|F=2\rangle \rightarrow |F'=2\rangle$, blue-detuned by δ_{rep}). Numerical values taken from [35].

cycle. For most alkali species, the excited state level spacing is large compared to the natural linewidth, and only a small fraction of the cooling laser power suffices for the repumping light.

For bosonic potassium, this is however not the case: The D2 transition manifold supplies the MOT transitions (see Fig. 3.2), out of which the $|F=2\rangle \rightarrow |F'=3\rangle$ transition is closed as the selection rules $\Delta F = 0, \pm 1$ forbid a relaxation to the $|F=1\rangle$ ground state. This makes it a suitable choice for the cooling transition. However, the hyperfine splitting of the $^2P_{3/2}$ excited state lies in the order of the natural linewidth $\gamma = 2\pi \times 6.035\,\text{MHz}$. Hence, atoms are excited to the $|F'=1,2,3\rangle$ states with comparable rates and many atoms are pumped to the $|F=1\rangle$ ground state, where they are dark for the cooling laser and the cooling process ceases to work after a few scattering events. The $|F=1\rangle \rightarrow |F'=2\rangle$ transition is suitable as a repumping frequency to pump atoms back to the right $|F=2\rangle$ ground state. Due to the high loss rate into the $|F=1\rangle$ ground state, both frequencies need to have comparable intensities. Hence, cooling and repumping beams take equal part in the deceleration and trapping of the atoms.

The tight excited level spacing gives rise to another problem: When the cooler is detuned by only a few linewidths to the $|F'=3\rangle$ upper state, it is simultaneously blue-detuned to the $|F'=0,1\rangle$ states. This results in a heating which counteracts the Sisyphus cooling mechanism. Because this does not allow the atoms to reach a sufficiently low temperature that is required

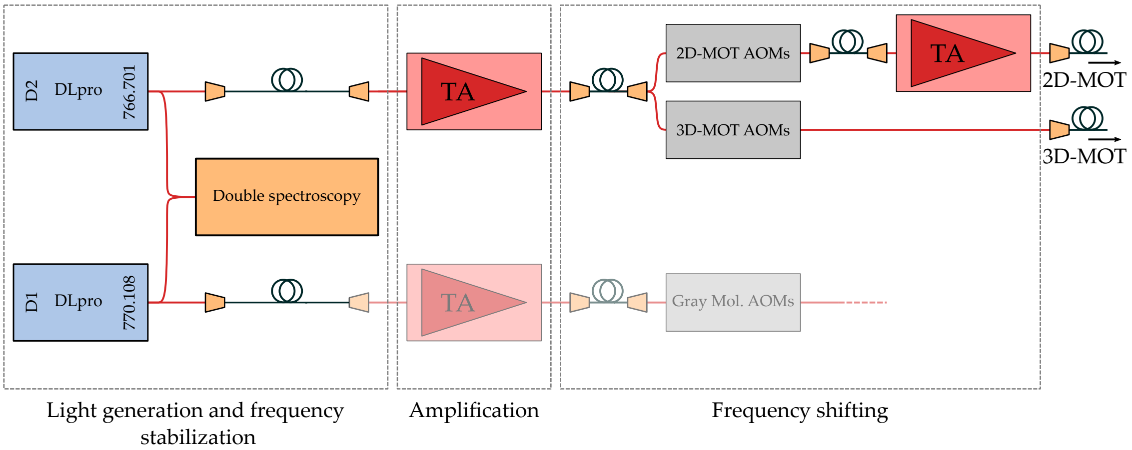

Figure 3.3: Overview of the laser system. The system can be split into three entities: In the first part, the D1 and D2 light is generated by ECDLs and stabilized using Doppler-free spectroscopy. Next, the light is amplified in a TA stage. In the third part, several AOMs generate the repumping and cooling frequencies for 2D- and 3D-MOT, before the light is finally sent to the experiment. The faded parts of the gray-molasses light are not set up yet.

for an efficient evaporation, an additional gray molasses is employed on the D1 line. The cooling light is blue-detuned with respect to the $|F = 1\rangle \rightarrow |F' = 1, 2\rangle$ transitions, which both result in gray molasses cooling. An additional repumper counteracts the depumping of atoms to the $|F = 2\rangle$ hyperfine ground state.

3.2 Overview of the Laser System

An all-diode laser system is a very cost-effective and stable solution to provide the D2 light required for the magneto-optical traps and the D1 light for the gray molasses. Figure 3.3 shows a schematic illustration of the different parts of the laser system. The basis is formed by two Toptica DL-Pro external cavity diode lasers, which are tuned to the D1 and D2 atomic transitions in ^{39}K. The lasers are frequency-locked to the crossover transitions via Doppler-free saturation spectroscopy. In a next step, the generated light is amplified in a tapered amplifier stage. Several acousto-optic modulators are then used to set the detunings for the MOT beams and generate the repumping and cooling frequencies. Single-mode optical fibers carry the light to the vacuum chamber. The individual parts of the laser system for 2D- and 3D-MOT are described in the following sub-chapters.

3.3 Light Generation

The performance of the magneto-optical traps is highly dependent on stability and precise tuning of the laser light. This places two challenges on the laser system: The linewidth has to be as narrow as possible, allowing for a precise addressing of a specific hyperfine transition,

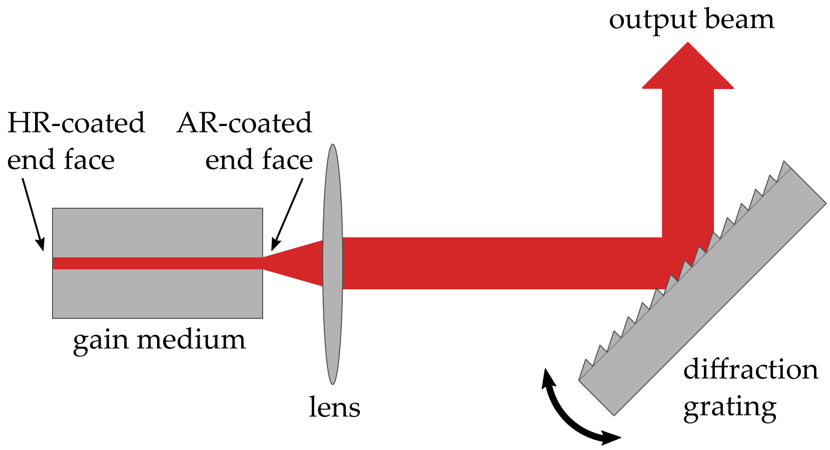

Figure 3.4: External cavity diode laser (ECDL) in Littrow configuration. The semiconductor chip is coated with a high-reflective (HR) and an anti-reflective (AR) surface. The laser cavity is externally completed by a diffraction grating as a wavelength-selective element. The first-order diffracted beam provides feedback to the resonator. By varying the grating angle, the laser frequency can be tuned.

and the frequency has to be tunable to account for drifts. A conventional laser diode can have a linewidth of several gigahertz, and the frequency is only coarsely adjustable via injection current and temperature. Both challenges can be overcome by using an *external cavity diode laser* (ECDL) [36–38].

In a conventional higher power ($\sim 100\,\mathrm{mW}$) semiconductor diode laser, rear and front facets of the gain medium are coated with a high reflector and an output coupling mirror, thereby closing the resonant cavity. In contrast to that, an ECDL uses a laser diode which features only the high reflector, while the front facet is anti-reflection coated. The cavity therefore needs to be closed by an external element. The Littrow configuration (see Fig. 3.4), for example, consists of a collimation lens and a diffraction grating as the end mirror. Optical feedback to the gain medium is provided by the first-order diffracted beam, while the reflected beam is coupled out of the cavity. A longer cavity increases the quality factor of the laser resonator which leads to a narrowed linewidth and a stabilized output. Because the diffraction grating acts as a wavelength-selective element, the emission frequency can be tuned by changing the grating angle.

As the laser has to be stabilized to an accuracy better than the natural linewidth, a well-established method is to obtain a spectrum of the given atomic species in which the hyperfine structure is resolved, and supply this signal as a frequency normal to a feedback loop controlling the laser frequency. However, plain laser absorption spectroscopy is unable to provide the required resolution. Due to various broadening mechanisms, the observed linewidths are much larger than the natural linewidth. The most important mechanism is *Doppler broadening*, which arises from the finite velocity of the atoms and translates the thermal velocity

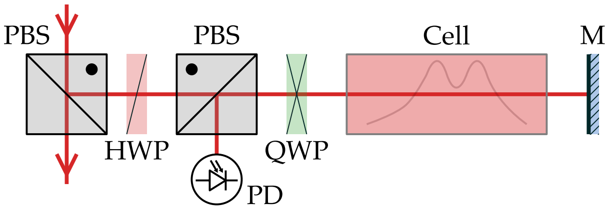

Figure 3.5: Optical setup for saturated absorption spectroscopy. A small part of the laser beam is sent to the spectroscopy path and passes through the glas cell before being retroreflected. A combination of a quarter wave plate and a polarizing beamsplitter sends the backwards traveling ray to a photodiode. Abbreviations used: PBS - Polarizing beamsplitter, HWP - Half-wave plate, QWP - Quarter-wave plate, PD - Photodiode, M - Mirror.

distribution via the Doppler shift $\Delta = kv$ into a Gaussian frequency distribution of width

$$\sigma_\omega = k\sigma_v = k\sqrt{\frac{k_B T}{M}}. \tag{3.1}$$

The Doppler broadening increases the natural linewidth of the ^{39}K D2-line at a temperature of $T = 70\,°\mathrm{C}$ to $\sigma_\omega = 2\pi \times 352.78\,\mathrm{MHz}$, which is two orders of magnitude higher than the natural linewidth. This makes it impossible to resolve the hyperfine structure. A way to overcome the broadening is Doppler-free saturation spectroscopy, which allows to resolve hyperfine transitions even at room temperature.

3.4 Doppler-free Saturated Absorption Spectroscopy

Saturation spectroscopy uses the saturation of the absorption for large intensities (cf. Eq. 2.12) to generate a Doppler-free signal. The core idea is to split the laser beam and send the partial beams anti-parallel through a spectroscopy cell. This can for example be accomplished with an optical setup as depicted in Fig. 3.5.

For a general picture, an atom in the spectroscopy cell can again be approximated as a two-level system. The forward traveling beam (*pump beam*) excites atoms with a velocity $v_\parallel = (\omega_L - \omega_0)/k$, removing them from the ground state population (*hole burning*). Due to the negative Doppler shift, the backward traveling beam (*probe beam*) excites atoms with the opposite velocity $v'_\parallel = -(\omega_L - \omega_0)/k$. When the laser frequency ω_L is far away from the resonance at ω_0, both laser beams interact with different velocity classes of atoms (see Fig. 3.6, outer graphs). Only when the laser frequency is near resonance, both beams interact with the same velocity class of atoms, exactly with those of $v_\parallel \approx 0$ (see Fig. 3.6, inner graph). If the intensity of the pump beam is chosen such that it saturates the transition, the hole burned into the ground state population leads to a reduced absorption for the probe beam, which can be observed as a narrow transmission peak (*Lamb peak*) inside the Doppler-broadened absorption dip (*Doppler valley*). The width of this Lamb peak is determined by the remaining broadening mechanisms such as pressure- and power-broadening.

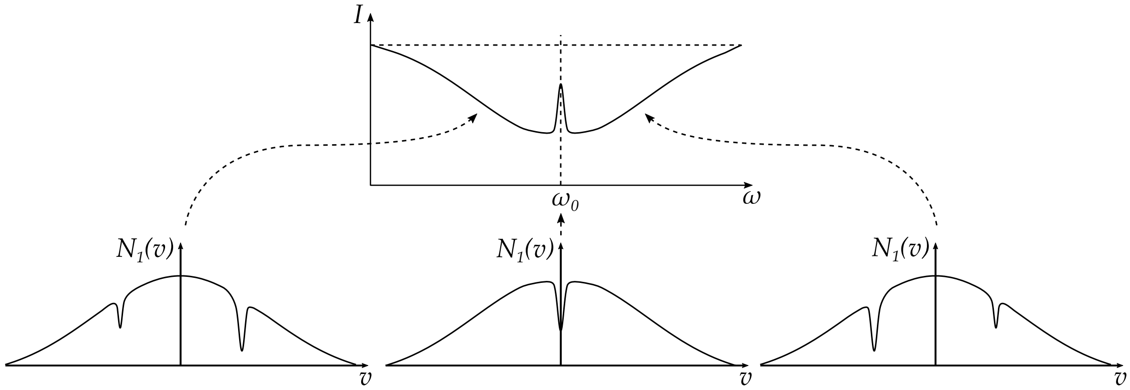

Figure 3.6: Hole burning in saturated absorption spectroscopy. With saturation due to the pump beam, a narrow Lamb peak emerges at the resonance frequency ω_0 out of the Doppler valley. The lower graphs depict the ground state population as a function of the velocity. The pump and probe beams burn a hole in the population, while only for atoms of velocity class $v = 0$, a Lamb peak is formed. Adapted from [24].

When a saturated absorption spectrum is taken, usually more than only the expected Lamb peaks for each atomic resonance can be observed. This phenomenon occurs when two transitions with frequencies ω_1 and ω_2 share a common upper or lower state (that is, a three-level system in V- or Λ-configuration), and have a frequency separation $\omega_2 - \omega_1$ smaller than the Doppler width. If the laser has a frequency equivalent to the arithmetic mean of the transition frequencies $\omega_L = (\omega_1 + \omega_2)/2$, the pump beam excites a certain velocity class on the ω_1 transition, while the probe beam excites the same velocity class on the ω_2 transition. Figure 3.7 indicates the velocity classes which are excited by the pump and probe beams as the laser frequency is scanned. Due to the opposite Doppler shift, the traces for the probe beam have the negative slope of the pump beam traces. Both beams cross at the atomic resonances at velocity $v = 0$ as expected. However, there are additional crossing points at a frequency in the middle between both resonances. These crossings result in an increased probe transmission, and additional peaks show up in the saturation spectrum (*cross-over resonances*). The signal is negative (dip) when the transitions share a common lower level, and positive (peak) when they share a common upper level. Crossover resonances are often more pronounced than individual Lamb peaks, because a higher number of atoms is simultaneously resonant (the crossover is resonant with two velocity classes, v_{co} and $-v_{co}$).

Laser frequency locking

Saturated absorption spectroscopy provides the possibility to resolve the hyperfine splitting of a given atomic resonance. The ultimate goal is to set the laser frequency to one specific resonance and correct for drifts away from the setpoint. However, due to the symmetry of the Lamb peaks, a conventional spectroscopy signal is only able to report the magnitude of the deviation, but not the direction. The laser controller therefore has no information on whether

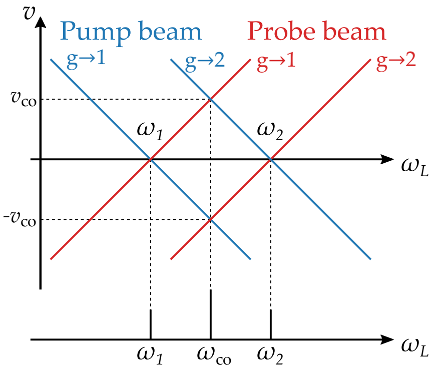

Figure 3.7: Origin of crossover resonances in saturation spectroscopy. The blue (red) lines show which velocity class the pump (probe) beam excites as the laser frequency is scanned. When more than one hyperfine transition lies in the Doppler valley, cross-excitations of pump- and probe-beam into different levels lead to the occurrence of additional peaks.

it has to decrease or increase the emission frequency. This can be overcome by using the derivative of the atomic resonances instead. The derivative has a zero-crossing at the atomic resonance and the vicinity is approximately linear. Hence, it contains information about both the magnitude and the direction of the deviation from the setpoint zero-crossing. This line can be seen as an error signal, allowing for a correction using a feedback loop.

A signal proportional to the derivative of the resonances can be generated by frequency-modulating the light in a saturated-absorption setup. This *FM-Spectroscopy* can, for example, be accomplished by modulating the laser current, which leads to additional sidebands at frequencies $\omega_C \pm \omega_{LO}$, where ω_C is the carrier frequency and ω_{LO} the modulation frequency. The modulated light passes the spectroscopy setup and the transmitted probe intensity is captured by a photodiode. Next, the signal on the photodiode is supplied to a *lock-in amplifier*. A lock-in amplifier combines a high signal-to-noise ratio amplification with phase-sensitive detection. By mixing the detected signal with the reference modulation signal and filtering out the fast oscillating terms with a low-pass filter, the amplifier generates a DC signal. This output signal depends on the relative phase shift between the different frequency components and is, for the right phase setting, proportional to the derivative of the input signal.

In a final step, the generated error signal is supplied to proportional/integral (P/I) regulators. The output of the PI regulators is attached to the piezo actuator controlling the grating angle, which closes the feedback loop. As long as the laser frequency stays inside the linear control region, the PI regulators are able to correct for any deviations, and the laser is locked to the atomic resonance.

Experimental realization

Figure 3.8 shows the optical setup for the D1 and D2 saturated absorption spectroscopies. The spectroscopy cell is embedded in a brazen cylinder, which is heated to about 70 °C. Due to the low vapor pressure of potassium, this is required to achieve a sufficiently high absorption. To

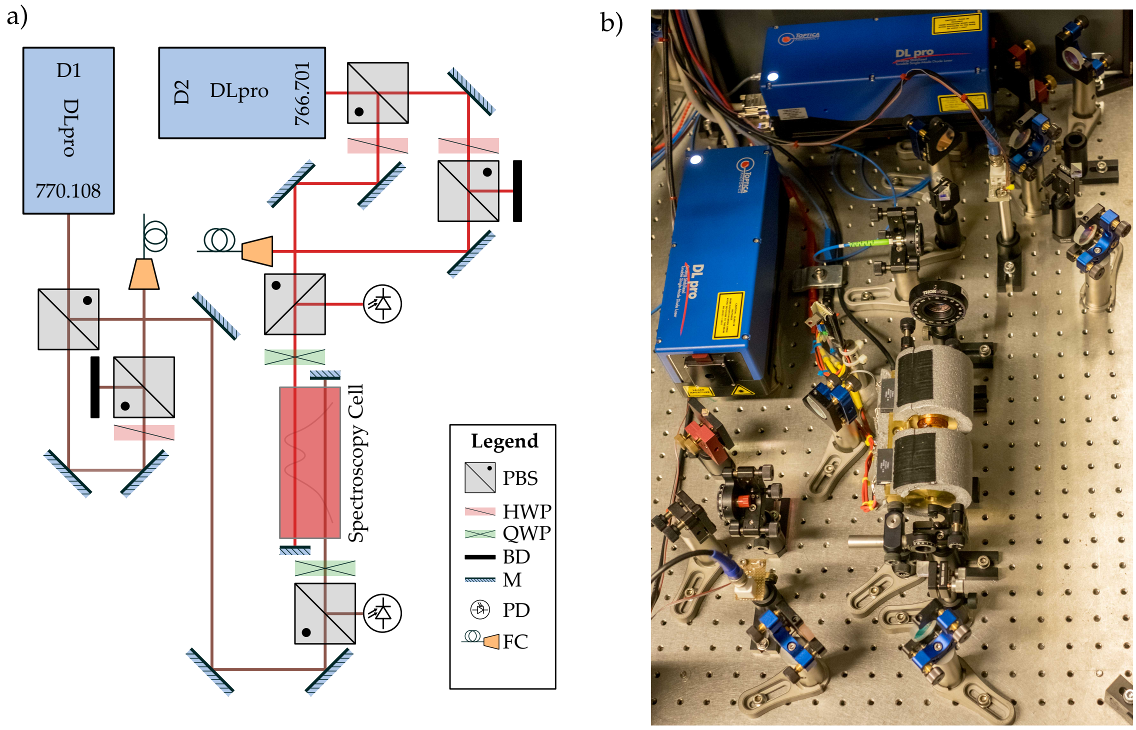

Figure 3.8: D1 and D2 spectroscopy. a) Schematic of the optical path. The main part of the laser light is coupled into single-mode fibers, while a small part is sent into the spectroscopy cell. With the help of half mirrors, one cell can be used for both frequencies. Abbreviations used: PBS - Polarizing beamsplitter, HWP - Half-wave plate, QWP - Quarter-wave plate, BD - Beam dump, M - Mirror, PD - Photo diode, FC - Fiber coupler. b) Picture of the aligned optical setup. The space on the right side has been left free for an AOM path.

avoid condensation of the alkali on the windows of the glass cell, the brazen housing covers the windows of the cell, leaving only a hole to transmit the laser beams free (see Fig. 3.8b). Additionally, the housing is open in the middle of the cell to shift the coldest point from the windows to the center.

For the locking technique, a frequency modulation is required. The usual approach of modulating the frequency via the laser current has the disadvantage that the light is modulated in the remaining parts of the experiment as well. In order to circumvent this, the Zeeman effect is used to imprint the modulation only on the light in the spectroscopy path. For this purpose, a copper coil is wound around the glass cell. When a modulation current ($\sim 100\,\mathrm{kHz}$) is applied to the coil, the Zeeman effect translates the oscillating current into a frequency modulation of the absorption signal, leaving the laser light outside the spectroscopy path unchanged.

In the experiment, it turned out that pump and probe beams had to be circularly polarized in order for this FM scheme to work. Because linear polarized light excites only π-(“vertical”) transitions with $\Delta M = 0$, the Zeeman shift causes an amplitude modulation (collective vertical motion) of the Lorentzian profile instead of the required frequency modulation (collective horizontal motion). Thus, the lock-in amplifier is unable to generate an error signal.

By using D-shaped half mirrors on either side of the spectroscopy cell, the D1- and D2-transitions can be simultaneously probed. A small part of the laser light is supplied to the spectroscopy, while most of it is coupled into single-mode fibers. Combinations of a PBS and a half-wave plate in front of the fibers allow for a variation of the coupled power. The D1 and D2 pump beam powers were adjusted to be 250 µW, corresponding to an intensity of $8.33\,\mathrm{mW\,cm^{-2}}$ (using an elliptical beam profile of $3\,\mathrm{mm}\times 1\,\mathrm{mm}$). These intensities are equivalent to a saturation parameter s_0 of 4.8, causing a power-broadening by a factor of about two. Reducing the power further did not lead to an increased resolution, because electronic noise becomes increasingly limiting for low intensities.

Figure 3.9 shows the saturated absorption spectrum for the D2-line, including the generated error signal. The phase settings of the lock-in amplifier have been optimized for maximum dynamic range on the crossover resonance. The large dip in the center corresponds to the ground-state crossover, and the two symmetric transitions can be identified by their intensities. The $|F = 1\rangle$-substate has three degenerate magnetic substates, whereas the $|F = 2\rangle$-substate has five, and should thus be more pronounced. The left peak can therefore be identified with the $|F = 2\rangle \rightarrow |F' = 1, 2, 3\rangle$ set of transitions, and the right peak with the $|F = 1\rangle \rightarrow |F' = 0, 1, 2\rangle$ set. The hyperfine splitting of the $^2\mathrm{P}_{3/2}$ excited state is too narrow to be resolved, resulting in one single peak. Using numerical values for the different level splittings, the x-axis can be calibrated to frequency units. Given this information, one can also understand why the left feature has a slightly dispersive shape instead of a discrete peak. The $^{41}\mathrm{K}$ isotope (orange lines) has its ground state crossover superimposed on the $^{39}\mathrm{K}$ transition line, accounting for the observed dip.

The D1 saturated absorption spectrum and the corresponding error signal is shown in Fig. 3.10. Because the splitting of the $^2\mathrm{P}_{1/2}$ excited state hyperfine structure is significantly larger than the $^2\mathrm{P}_{3/2}$ splitting, all four levels of the D1 manifold can be resolved. This yields several observable crossover transitions, which can best be described by modifying Fig. 3.7. The result in Fig. 3.12 indicates nine observable transitions, occurring as characteristic triplets. Identifying the left peak with the $|F = 2\rangle \rightarrow |F' = 1, 2\rangle$ set of transitions and the right peak with the $|F = 1\rangle \rightarrow |F' = 1, 2\rangle$ set, this allows to calibrate the frequency axis and mark all occurring transitions. It is interesting to note that power broadening is indeed limiting the resolution of this method, as an increase of the pump beam power by a factor of three led to a dissolution of the finer structures.

Because the cooling light for the MOTs needs to be locked on the $|F = 2\rangle \rightarrow |F'\rangle$ and the repumping light on the $|F = 1\rangle \rightarrow |F'\rangle$ transition, the crossover resonance is a perfect choice for the locking point. The necessary frequencies can then be reached using two acousto-optic modulators with a shift of $\pm 238.5\,\mathrm{MHz}$.

A typical locking procedure for the D2 transition is shown in Fig. 3.11. First, the crossover transition is positioned to the center of the scanning region by changing the average piezo voltage. The scanning range is then decreased while continuously correcting the centering.

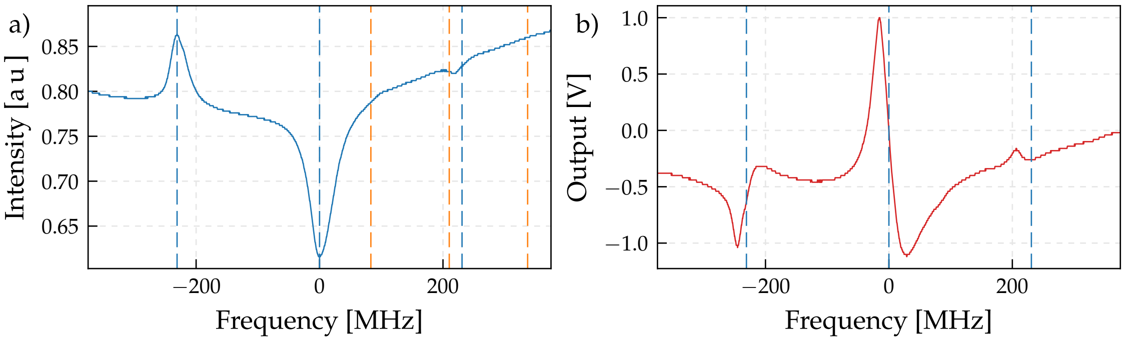

Figure 3.9: ^{39}K D2 Saturated absorption spectrum. a) Spectroscopy signal. The centered dip is the ground state crossover, the left peak the $|F = 2\rangle \rightarrow |F' = 1, 2, 3\rangle$ set of transitions, and the right peak the $|F = 1\rangle \rightarrow |F' = 0, 1, 2\rangle$ set. The frequency scale has been calibrated using numerical values for the hyperfine splitting, the blue (orange) dashed lines mark the transitions in ^{39}K (^{41}K). b) Generated error signal. The lock-in amplifier has been optimized for maximum dynamic range on the crossover resonance.

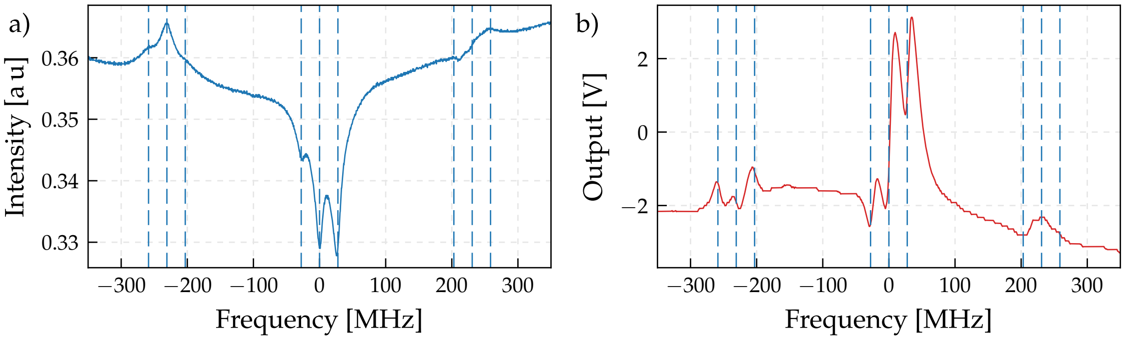

Figure 3.10: ^{39}K D1 Saturated absorption spectrum. a) Spectroscopy signal. The centered dip is the ground state crossover, the left peak the $|F = 2\rangle \rightarrow |F' = 1, 2\rangle$ set of transitions, and the right peak the $|F = 1\rangle \rightarrow |F' = 1, 2\rangle$ set. The frequency scale has been calibrated using numerical values for the hyperfine splitting, the blue dashed lines mark the transitions in ^{39}K. b) Generated error signal. The lock-in amplifier has been optimized for maximum dynamic range on the crossover resonance.

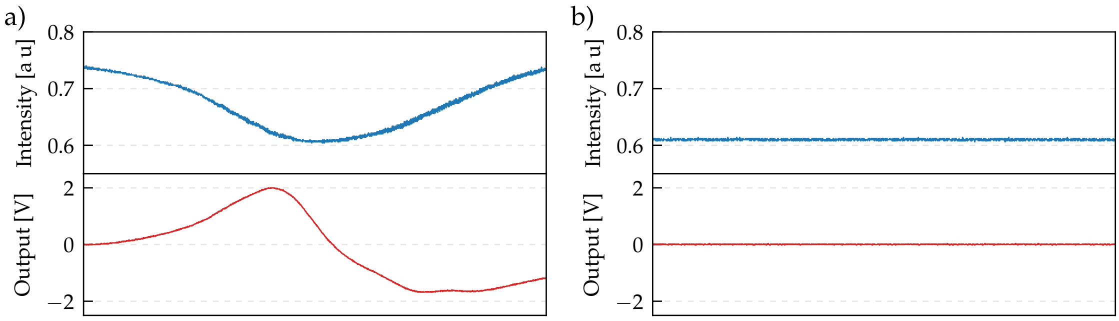

Figure 3.11: Locking procedure for the D2 ground state crossover. a) The ground state crossover is centered with respect to the scanning region, and the scanning range is subsequently diminished. b) The PI-regulator is activated, and the laser is locked to the transition.

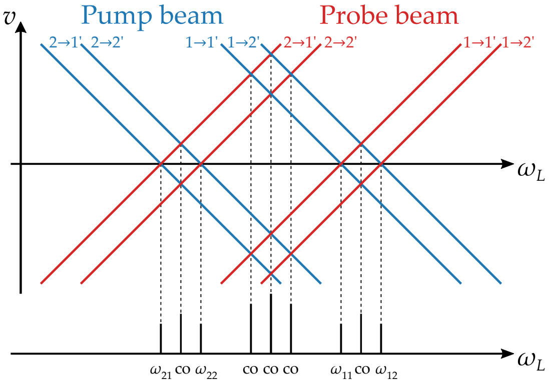

Figure 3.12: Crossover resonances for the D1 line. Because the D1 transition manifold consists of four energy levels that all have a sufficient separation, a total of nine lines is observed - the four expected atomic resonances and five additional crossovers.

Additionally, the region of linear slope in the error signal has to be centered on the voltage-axis (Fig. 3.11a). When the scanning range is minimal, both the photodiode and error signals should have a vanishing slope. Now, the control loop can be activated. The laser is locked to the transition when the photodiode intensity remains at the same value and the error signal vanishes (Fig. 3.11b).

3.5 Tapered Amplifiers

The frequency-stabilized light from the ECDLs has a power smaller than 100 mW. To drive the magneto-optical traps, the power of the light has to be further increased by an amplifier which keeps its spectral characteristics. For this, a tapered amplifier can be used.

A *Tapered Amplifier* (TA) is a semiconductor device for amplifying the power of an incoming laser beam (*seed beam*) from a few milliwatt to several watt. While the basic principle is similar to that of a semiconductor laser diode, the end faces are anti-reflection coated and thus, no cavity is formed. Additionally, the width of the gain medium increases over the length of the chip. This reduces the power density inside the semiconductor and allows high output powers. The structure of a typical TA diode is shown in Fig. 3.13a. An electrical current enters the metallic contact pad (light orange) and runs downwards through the semiconductor layers (gray) to the active region (red), where the light is amplified. The shape of the contact pad defines the amplification region (*gain guiding*).

The seed beam enters the TA on the side of the ridged waveguide. The ridged waveguide is long and narrow, filtering out only a single mode of the seed radiation. This mode enters the tapered waveguide and is subsequently amplified, before exiting the TA through the large output aperture (usually $\sim 200\,\mu\text{m}$ wide). In order to achieve sufficient amplification, the carrier inversion inside the active region has to be large. This leads to an increase in spontaneous emission, which in turn is also amplified (*amplified spontaneous emission*, ASE). Hence, the output beam has two contributions: The amplified seed signal and a broad ASE

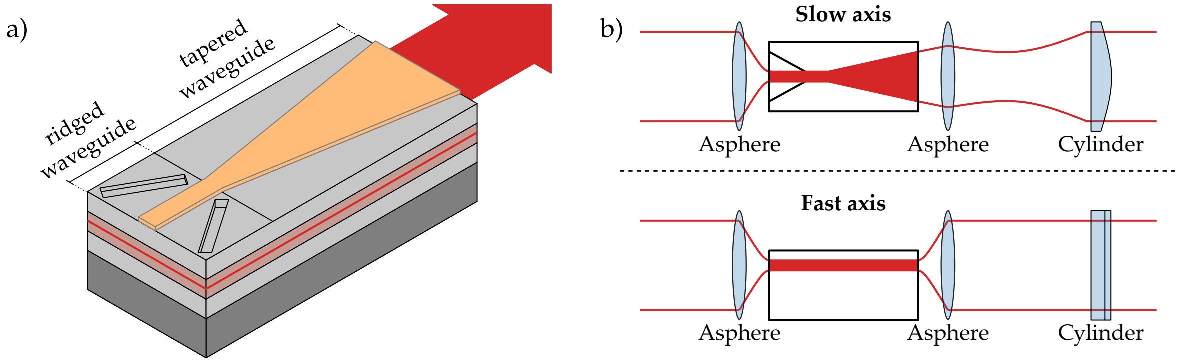

Figure 3.13: A tapered amplifier diode. a) Schematic of a semiconductor tapered amplifier chip. The active region is made of a ridged waveguide and a tapered amplification area. b) Due to the geometry of the active layer, the output beam is elliptical and has vastly different divergences, requiring for a combination of an aspherical lens and a cylinder lens to collimate its slow and fast axes.

background, which is increasingly suppressed with higher seed powers. The advantage of the TA is that it conserves the characteristics of the seed beam. In combination with an ECDL, large output powers of spectrally narrow and stable laser radiation can be obtained. Due to the rectangular shape of the emission region, the output beam spreads with vastly different divergences in horizontal and vertical direction (see Fig. 3.13b). The vertical direction has the higher divergence, and is therefore called the *fast axis*. To maintain a small output beam, it has to be collimated by a short focal length lens with low spherical aberrations. The horizontal direction, or *slow axis*, has a lower divergence, which is mainly determined by the taper angle. Because it is already pre-focused by the first lens, a cylindrical lens can be used to collimate this direction without altering the beam along the fast axis.

Custom tapered amplifier module

A custom tapered amplifier module was designed by Florian Nicolai in his master's thesis [39]. The aim of this module was to have an independent, fiber-coupled setup that can be easily adapted for different purposes. The layout of the amplifier module is shown in Fig. 3.14. The seed side consists of a fiber collimator and two guiding mirrors.

The first element on the output side is a $f = 40\,\mathrm{mm}$ cylindrical lens to collimate the slow axis. Right behind the cylindrical lens, a Faraday isolator allows light to pass only in one direction, while the opposite direction is strongly attenuated. This element is critical for a stable and safe operation. As the amplification can occur in both directions, a back-reflection of only a few milliwatts leads to an enormous power density on the small input facet, irreparably damaging the semiconductor chip. Additionally, weaker reflections can lead to output intensity fluctuations and mode-hopping, which would make the tapered amplifier unusable as a stable laser source.

The output side is terminated by two guiding mirrors and a fiber coupler to couple the

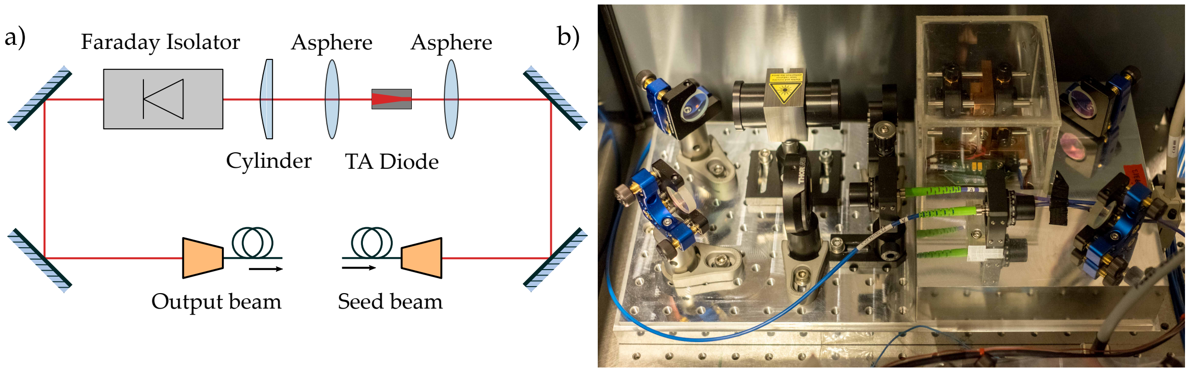

Figure 3.14: Setup of the custom tapered amplifier module. a) Schematic drawing of the TA module. A fiber collimator and two guiding mirrors make up the seed side. The output side consists of a $f = 40\,\mathrm{mm}$ cylindrical lens, a Faraday isolator, two guiding mirrors and a fiber coupler. Both fiber ports use a $f = 13.86\,\mathrm{mm} asphericlens$. b) A completely aligned TA module. The components are fixed on a milled aluminum baseplate, and the TA diode is mounted on the copper block. The TA diode is protected from thermal fluctuations and acoustic noise by a plastic enclosure. An additional enclosure (not shown) protects the complete module.

light into a single-mode fiber. All components are fixed on an aluminum baseplate. The TA chip used is a model EYP-TPA-0765-02000 by Eagleyard Photonics with a maximum optical power of 2 W and a center wavelength of 765 nm. It is housed in a copper block to ensure good thermal contact (see Fig. 3.15a). Four clearance holes, which are milled such that the amplifier chip is in their center, allow the attachment of two $f = 4.51\,\mathrm{mm}$ aspherical lenses on XYZ translation mounts. Lenses with focal lengths of $f = 13.86\,\mathrm{mm}$ for both fiber collimator and coupler result in a suitable matching to the input and output modes of the used amplifier chip. A drawing of the baseplate indicating the placement of the components with exact dimensions is enclosed in the Appendix (Fig. A.2).

Alignment procedure

The seed beam has to be focused on the input facet of the amplifier chip, which has a width of only 3 µm. Additionally, the axis of the seed beam must overlap the optical axis of the chip to a very high degree. Unless both requirements are fulfilled, no amplification occurs. Hence, a special alignment procedure is necessary, which will be described in the following.

The alignment begins with only the TA copper block mounted on the aluminum baseplate (see Fig. 3.15a). A current of approximately 1000 mA is supplied to the chip, leading to a visible ASE signal emerging from both facets. Using the z-axis screw on the aspheric lens mounts, the vertical direction of the ASE is collimated on a screen sufficiently far away from the chip. The centering of the aspheric lenses with respect to the chip facets is critical for a good output mode. In order to achieve this, a custom alignment tool has been constructed, consisting of a cage plate, a lens tube and an iris (see Fig. 3.15b). The cage plate can be attached to the cage rods, whose center coincides with the optical axis of the chip. Therefore, the center

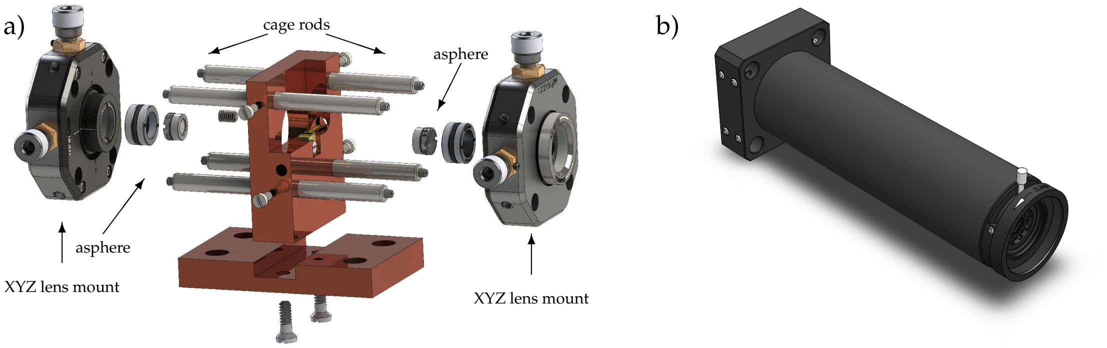

Figure 3.15: Alignment of the TA copper block. a) Copper block which houses the TA diode. Four cage rods ensure the centering of the asphere mounts relative to the optical axis of the chip. From [39]. b) Alignment tool for centering the aspheric lenses. The tool consists of a CP02T/M cage plate, a 4" lens tube and a SM1-threaded iris from Thorlabs. It is mounted directly on the four cage rods of the TA copper housing.

of the iris is automatically aligned with the input facet. By iteratively lowering the aperture and centering the ASE through the iris using the X-/Y-screws on the lens mount, the aspheric lenses can be centered to the chip axis.

In the next step, the seed side is aligned. After the fiber collimator has been properly set up, it is mounted on the base plate together with the two guiding mirrors. The seed beam and the ASE are now overlapped over the whole path. Two positions along the beam path with a maximum distance are chosen, e.g. in front of the fiber collimator and the seed asphere. At each position, the beams are overlapped with the help of a thin paper sheet (e.g. a lens cleaning tissue) in an iterative process. When the seed beam is unblocked, a large increase in output power should be observed. If this is not the case, slight adjustments to the seed mirrors while supervising the TA output usually help. From this point on, extreme caution should be taken. The optical power on the output side can now already measure more than a hundred milliwatts. Coarse adjustment should thus only be done with considerably reduced output power.

The first step in aligning the output side is to place the Faraday isolator into the beam path, leaving enough space for the cylindrical lens. The locking screw for the isolator tube is loosened, and the tube is rotated until a maximum in transmitted power after the isolator is observed. The position of the beam is marked on a screen sufficiently far away. Next, the cylindrical lens is put in place, while the height and the horizontal displacement is adjusted such that the beam is centered on the marking points. The distance of the cylindrical lens from the amplifier chip is varied until the beam is also collimated in horizontal direction. With the two guiding mirrors put in place, the pre-collimated fiber coupler is mounted on the aluminium plate. The coupler should not be placed directly in front of the seed collimator to leave enough space for the fiber.

The optical power after the Faraday isolator should now be adjusted to about 10 mW by varying the amplifier current. Using the two guiding mirrors, the light is coupled into the output fiber. As a next step, the beam divergence is matched to the output coupler by turning the z-positioning screw on the output asphere and tuning the guiding mirrors after each step. When a maximum with a coupling efficiency of more than 50 % has been found, the power in front of the fiber can be slowly increased to about 500 mW. As before, the coupling efficiency is maximized via the guiding mirrors. As the injection current is increasing, the TA diode and its copper mount heat up and expand. This can be corrected by readjusting the seed mirrors. The precision adjustment knob on the cylinder lens allows to tune the collimation of the slow axis. After each full rotation of the knob, the fiber coupling is readjusted and a maximum in coupling efficiency is searched for. Because the travel length is only 3 mm, it is likely that the maximum lies outside this range. In this case, the post clamp holding the cylinder lens has to be unlocked and the lens mount has to be manually moved. When a sufficient coupling efficiency has been achieved, the injection current can be slowly increased to its designated value. The previous adjustments are iterated until a maximum in coupling efficiency is observed. At such high output powers, all beam displacements must be done slowly to prevent a burning of the fiber head.

The output is coupled into polarization-maintaining single-mode fibers. In this special kind of fiber, stress rods are embedded into the cladding which cause birefringence in the core material. This prevents coupling of the two optical axes, and when the polarization of the coupled light is aligned to either of them, the fiber maintains the input polarization. Otherwise, the fiber acts as a high-order wave-plate whose retardation is highly dependent on temperature or stress. Whenever polarization-sensitive optics are placed behind the fiber, their behavior changes uncontrollably due to the fluctuating light polarization. It is therefore essential to ensure proper polarization-maintaining coupling.

Polarization-maintaining coupling can be achieved by placing a polarization-sensitive element after the fiber and observing intensity fluctuations. For this, a combination of a half-wave plate and a PBS was used. The half-wave plate is set to transmit around 50 % of the coupled power through the beam splitter to allow a maximum sensitivity. If the input polarization is not matched to the fiber orientation, slightly heating the fiber (by e.g. gripping it with a hand) leads to intensity modulations after the beamsplitter. By rotating the input polarization, the modulation amplitude is minimized.

The fiber couplers used in this setup are custom built from Thorlabs components. The coupling lens and the fiber adapter are connected to the SM1-cage plate housing by a nested rotation mount. Hence, the fiber can be rotated with respect to the light polarization. During the alignment, this approach proved to be inconvenient. Since the optical axis of the coupling lens does not necessarily coincide with the rotation center, even the slightest rotation will lead to almost no light being coupled into the fiber anymore. Because the optimal position is very narrow, the continuous recoupling makes the process extremely inefficient. Additionally, the misalignments lead to a considerable amount of light being launched into the fiber cladding,

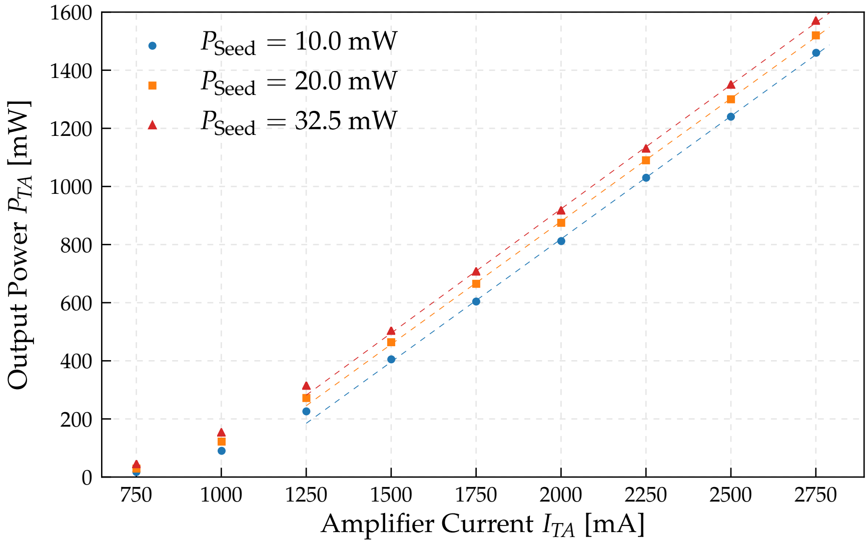

Figure 3.16: Output power calibration. Measured output power after the Faraday isolator as a function of the injection current for three different seed powers. Above a current of 1250 mA, the output is approximately linear. The Faraday isolator has a transmission of 80 %. The dashed lines are linear fits with a mean slope of 0.85 W/A.

which led to a burnt fiber tip in one case. When this happens, a sudden drop in coupling efficiency can be observed. Before the fiber can be reused, the tip has to be polished. To make the alignment much more efficient, an additional half-wave plate was placed directly in front of the fiber coupler. This allows a rotation of the input polarization without altering the beam angle or position.

Characterization and performance measurements

As a first step, the response of the output power as a function of the supplied injection current was analyzed. Figure 3.16 shows the measured output power directly behind the Faraday isolator for three different seed powers. All three traces exhibit a linear dependence for currents above 1250 mA with a slope of about 0.85 W/A. Taking into account that the Faraday isolator has a measured transmission of $T \approx 80\,\%$, this corresponds to a slope of 1.02 W/A, in good agreement with the manufacturer specification of 1 W/A. The recommended maximum optical output power of the diode is $P_{\mathrm{opt}}^{\mathrm{max}} = 2\,\mathrm{W}$. This corresponds to a power after the Faraday isolator of $P_{\mathrm{nom}} = 1.6\,\mathrm{W}$, which is the current value the amplifiers are operated at. The seed saturation is best analyzed by holding the injection current at a fixed value and recording the output power as a function of the seed power. The measurement in Fig. 3.17a indicates a clear saturation for seed powers above 25 mW, confirming that this is the region where maximum performance is achieved. Additionally, the response of the TA at very small seed powers was analyzed. Figure 3.17b shows that the slope of the P-I-curve decreases for low seed powers in comparison to Fig. 3.16. However, even for seed powers on the order of 100 µW, no current saturation is observable within safe operating conditions for the chip.

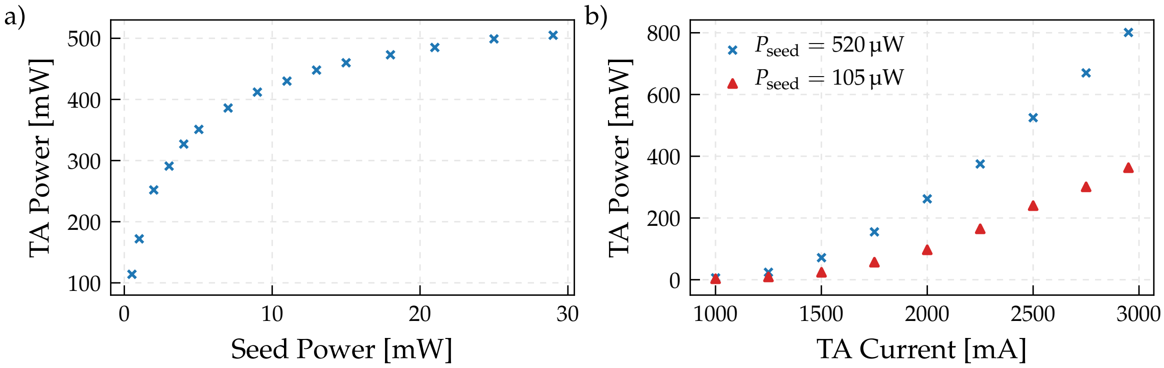

Figure 3.17: Power saturation of a TA. a) The output power of the TA shows a saturation behavior when varying the input seed power. The region of 0 to 5mW exhibits a strong increase in power, whereas the output saturates for seed powers larger than about 20 mW. Measured at $I_{\mathrm{TA}} = 1500\,\mathrm{mA}$. b) For very small seed powers on the order of 100 µW, the slope of the gain curve decreases. However, no current saturation can be observed within safe operating conditions for the chip.

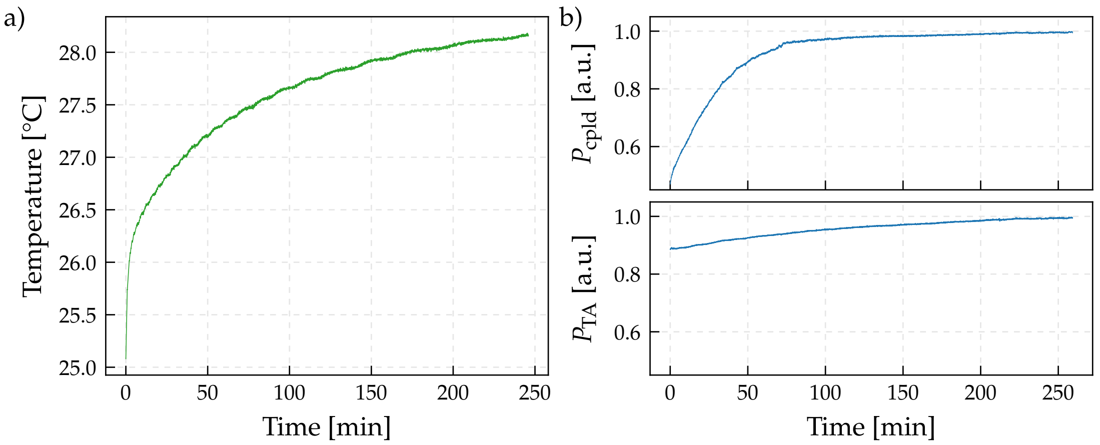

Figure 3.18: Startup behavior of a cold TA to nominal power. a) The temperature in the vicinity of the TA diode was measured using a thermistor inserted into a hole in the copper mount. The graph shows that the tapered amplifier needs more than 200 minutes to reach a steady-state temperature of about $T = 28.5\,°\mathrm{C}$, corresponding to an increase of about 3.5 °C from the laboratory temperature. b) The power behind the fiber (upper graph) and in front of it (lower graph) was measured as a function of time after a cold start. The values were normalized to their respective steady-state value and the axis scaling was chosen equally. The coupled power doubles while thermalizing, reaching a steady-state after about 100 minutes. The power in front of the fiber changes only by about 10 % and has a longer time constant, comparable with the temperature evolution. All measurements were recorded simultaneously.

The original design of the TA module included an active temperature stabilization using a thermoelectric cooler (TEC) sandwiched between copper mount and base plate. To simplify the setup, the possibility of a passive cooling was investigated.

The TEC was substituted by a milled copper plate for maximum thermal contact to the base plate. Figure 3.18a shows the temperature curve for a startup from room temperature to nominal output power. A thermistor inserted into a hole in the vicinity of the TA diode was used to record the temperature. The graph confirms safe operating conditions under passive cooling, since the vicinity of the amplifier chip only heats up by about 3.5 °C. However, the module reaches a steady-state temperature of about 28.5 °C only after more than 200 min. While this is impractical when a power cycling is required, the modules are going to run continuously and at a fixed current value in day-to-day operation. Additionally, the modules will be sealed by plastic enclosures from sudden temperature changes, which makes the passively-cooled approach a reasonable simplification. In order to characterize the evolution of the coupled power as a function of time, the power after (upper graph) and in front of (lower graph) the output fiber was recorded after a cold start (see Fig. 3.18b). The values were normalized to their respective steady-state values and an equal scaling was chosen to allow an easier comparison. The output power shows a steep rise during the first 70 minutes, nearly doubling its value. In contrast to that, the power in front of the fiber increases only by about 10 % over the whole measuring time, and has a much longer time constant comparable to the temperature curve. It is therefore very likely that the heating-up of the fiber coupler and the fiber itself have a significant influence on the coupled power. While no direct measurement of the temperature near the fiber tip has been performed, the aluminum plate housing the fiber adapter heats up noticeably during startup, confirming this hypothesis. Due to the large heat-sink volume of the chip mount, the effects of thermal expansion are less pronounced on the input side.

The cooling and repumping frequencies for 2D- and 3D-MOT require two tapered amplifier modules, which were set-up and adjusted in the course of this work. In agreement with the observations done in [39], the coupling efficiency is strongly dependent on the specific diode chip. The individual samples exhibit different output modes, which has a direct influence on the maximum achievable coupling efficiency. The diodes which were built into the two amplifier modules both showed a double-lobe structure – an intensity minimum in the beam center surrounded by two stripes of high intensity. Combined with an elliptical beam profile, the expected coupling efficiency lies significantly below that of a beam with a Gaussian intensity distribution. In the end, the module with chip serial number EA-07286 yielded a power after the single-mode fiber of 780 mW, corresponding to a coupling efficiency of about 49 %. The second module with serial number EA-07313 yielded 920 mW with a coupling efficiency of 58 %. The module with higher coupling efficiency will be used to supply the acousto-optic modulators, while the other one amplifies the frequencies for the 2D-MOT.

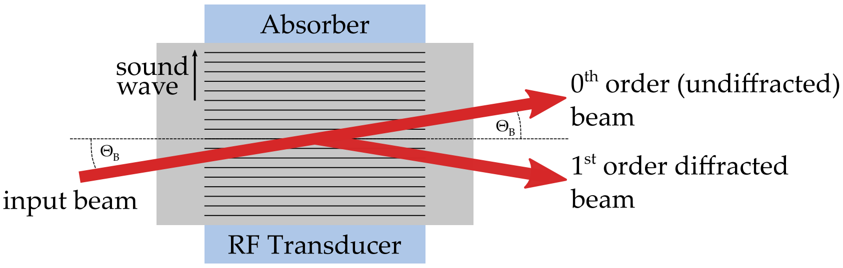

Figure 3.19: Schematic setup of an acousto-optic modulator. A crystal exhibiting the acousto-optic effect is sandwiched between an RF transducer and an absorber. The RF transducer generates a traveling density wave inside the crystal, which acts as a diffraction grating for incident light waves.

3.6 Acousto-Optic Modulators

The laser generating the light for the magneto-optical traps has been locked to the crossover transition of the ^{39}K D2-line. This frequency has to be shifted by $\pm 238.5\,\text{MHz}$ to drive the repumping and cooling transitions. Additionally, the scattering forces require a detuning, which has to be adjusted while maximizing certain parameters of the MOT. Such a variable frequency shifting can be done by means of an *acousto-optic modulator* (AOM).

An acousto-optic modulator is a device which incorporates a material exhibiting the acousto-optic effect (the variation of the refractive index by a sound wave) [40]. It can be used to modulate the frequency, power or spatial direction of a laser beam. The material is usually a transparent crystal (common are e.g. TeO_2 or crystalline quartz), sandwiched between a radio-frequency (RF) transducer and an absorber (see Fig. 3.19). The piezoelectric transducer produces a density wave inside the crystal that propagates with the sound velocity v_s and has a frequency Ω on the order of several hundred megahertz. This traveling density wave leads to a periodic refractive index grating inside the crystal. An incident laser beam of frequency ω can be treated as a photon with momentum k, which scatters with a phonon with momentum κ of the acoustic field. This scattering process leads to an absorption or emission of acoustic phonons. Momentum conservation dictates that the wave vector k' of the outgoing light wave is

$$k' = k \pm m\kappa, \tag{3.2}$$

while energy conservation requires for the frequency ω' of the outgoing wave

$$\omega' = \omega \pm m\Omega. \tag{3.3}$$

The sign depends on whether a phonon is absorbed and emitted, and m denotes the diffraction order (the amount of emitted/absorbed phonons). The conservation laws show that the diffracted light wave undergoes a change in both direction and frequency. Constructive

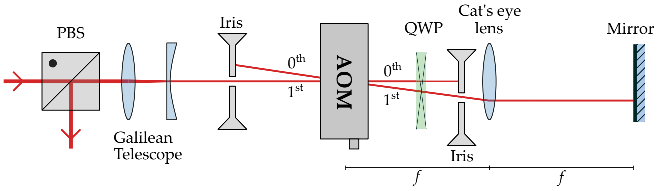

Figure 3.20: Double-pass AOM setup with cat's eye retroreflector. The diameter of the incident beam is decreased to match it to the acoustic aperture of the AOM. The first order diffracted beam is retroreflected for a second pass through the AOM, while the zeroth orders are blocked with an iris diaphragm. An additional cat's eye lens in the focus of AOM and mirror is used to increase the bandwidth. The frequency-shifted beam is separated from the incident beam by means of a quarter-wave retarder and a PBS cube. Abbreviations used: PBS - Polarizing beamsplitter, QWP: Quarter-wave plate.

interference for the diffracted rays is observed whenever the *Bragg condition*

$$\sin \Theta_B = \frac{m\omega}{2\Omega} \frac{c}{v_s} \tag{3.4}$$

is fulfilled, where c is the speed of light and v_s the speed of sound in the crystal. With the parameters on the right hand side usually known, the diffraction angle can be calculated.

The main purpose for AOMs in ultracold atom experiments is to shift the frequency of laser beams by a variable amount. By varying the angle between the AOM and the optical axis of the incident light, the amount of light that is diffracted into a specific order can be controlled. Hence, a careful alignment of the modulator gives rise to a very efficient frequency shifting.

Double-pass configuration with a cat's eye retroreflector

The change in beam direction due to the Bragg scattering is an unwanted side effect for many applications. When either the laser frequency is scanned or the AOM frequency is changed, the diffraction angle is modified according to Eq. 3.4. This leads to a misalignment of the optical paths downstream of the AOM. The change in diffraction angle can be effectively compensated by using the AOM in the *double-pass configuration*.

Figure 3.20 shows an example setup to achieve the double-pass. The beam passes a Galilean telescope to match the beam diameter to the acoustic aperture of the AOM. The 0^{th} order is blocked by an iris diaphragm, while the m^{th} order is retroreflected for a second pass through the AOM. The m^{th} order retroreflected beam is overlapping with the incident beam, independent of the AOM frequency. With the help of a quarter-wave plate in the beam path, the output beam can be separated from the input beam. Due to a second passage through the AOM, this configuration leads to a frequency shift of twice the single-pass shift.

As an addition to a double-pass setup itself, a *cat's eye retroreflector* is employed. It consists of a convex lens, placed a focal length away from the AOM and the retroreflector. Due to the lens, the beam always hits the mirror perpendicular to its surface. Because this is independent of the frequency shift, beam displacements are minimized. This leads to a significant increase in bandwidth as compared to a standard double-pass AOM [41].

Experimental realization

Because the detuning of cooler and repumper for 2D- and 3D-MOT must be adjusted independently, a total of four AOM paths is required. Figure 3.21 depicts the experimental realization of the AOM paths. The D2 light, locked to the crossover transitions in the spectroscopy setup, is amplified by the first TA module. It is then split into the four paths by polarizing beamsplitters, while the power can be individually adjusted for each path using half-wave retarders. After passing the double-pass AOM setups, repumping and cooling frequencies are mixed on a non-polarizing beamsplitter to maintain their polarization. The output of both splitters is coupled into single-mode fibers. The 3D-MOT light is directly sent to the science table, whereas the 2D-MOT is previously amplified by a second TA module.

During the construction, the choice of components was done to maximize the following three parameters: Diffraction efficiency, coupling efficiency and bandwidth. For the setup, acousto-optic modulators of the model AOMO 3110-120 from Crystal Technology, Inc. with a center frequency of 110 MHz were used. The manufacturer data-sheet specifies that for the given acoustic aperture of 2.5 mm × 0.6 mm (L×H), best diffraction efficiencies are achieved for beam waists greater than around 200 µm inside the crystal. The first approach was building a simple double-pass setup with a 1:1 Kepler telescope and the AOM placed in the focal point. Using Gaussian optics, the beam waist diameter d in the focal point can be estimated by

$$d = \frac{4\lambda F}{\pi D}, \tag{3.5}$$

where F is the focal length of the lens, λ the light wavelength and D the $1/e^2$ diameter for the collimated input beam. Using $D = 2\,\mathrm{mm}$, $\lambda = 766.701\,\mathrm{nm}$ and $F = 200\,\mathrm{mm}$, a focal beam diameter of about 100 µm is obtained. In agreement with the manufacturer specifications, the small beam waist lead to a maximum of about 70 % single-pass efficiency, while at least 85 % should be achievable. According to Eq. 3.5, a larger beam waist can be achieved by either reducing the input beam diameter or increasing the focal length of the lenses. A higher focal length is unpractical, since it would at least double the length of the AOM paths. When instead a smaller input beam diameter is used, the path along which the beam has a small diameter must be kept as short as possible. Otherwise, the inherently high divergence of a Gaussian beam with a small spot size significantly widens the beam and leads to reduced coupling efficiencies. To meet these requirements, the 1:1 Kepler telescope approach was omitted. Instead, the beam diameter is reduced in a Galilean telescope at the beginning of each AOM path. This way, the path along which the beam has a small spot size is sufficiently short to counteract a noticeable widening. Experimentally, a reduction factor of 3:1 proved to be a reasonable trade-off between diffraction efficiency and beam widening.

After adjusting the AOM paths, single-pass diffraction efficiencies of about 92 % and double-

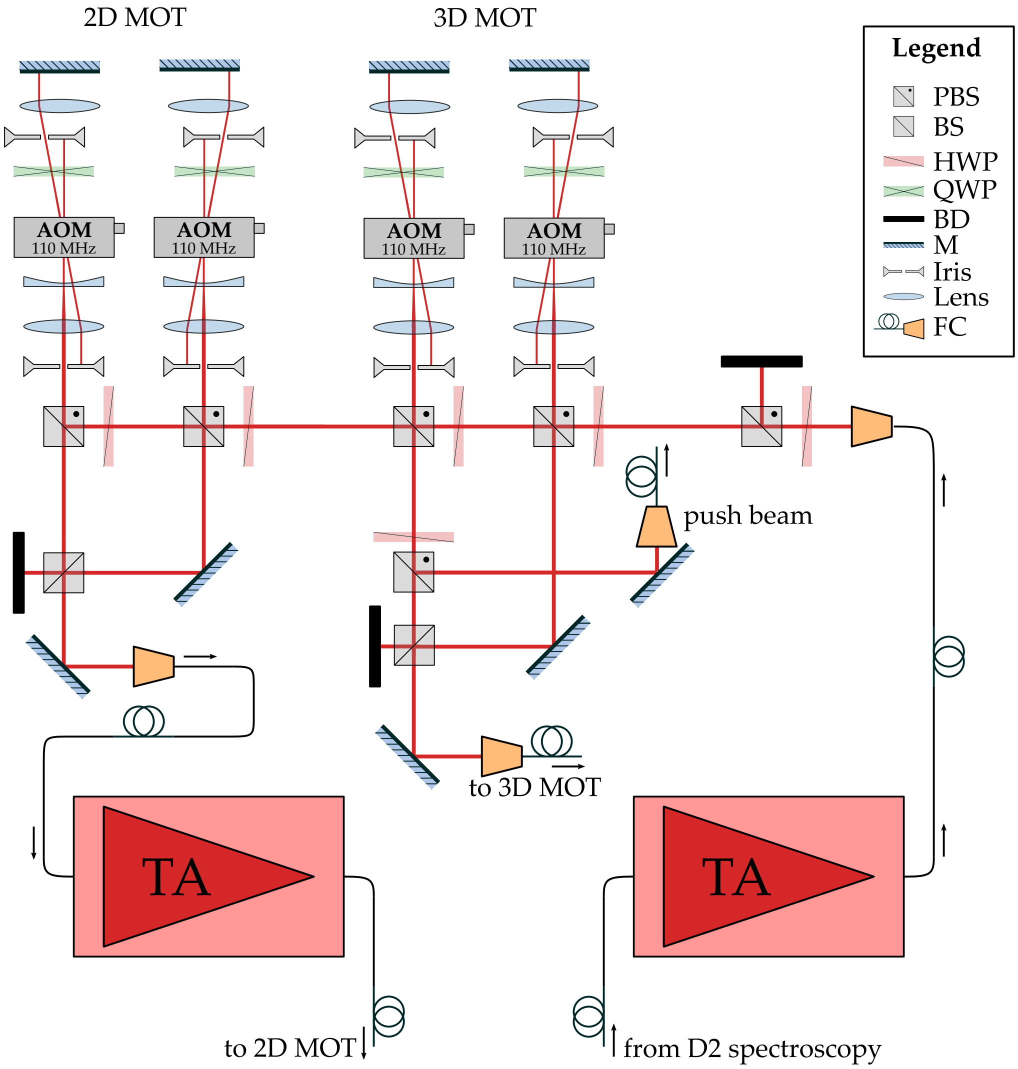

Figure 3.21: Experimental realization of the AOM paths. The D2 light from the first TA is split into four AOM paths, generating the cooling and repumping frequencies for the 2D- and 3D-MOTs, respectively. For each MOT, the two frequencies are united by means of non-polarizing beamsplitters and coupled into single-mode fibers. The 3D-MOT light is sent directly to the experiment, while the 2D-MOT light is previously amplified in a second TA.

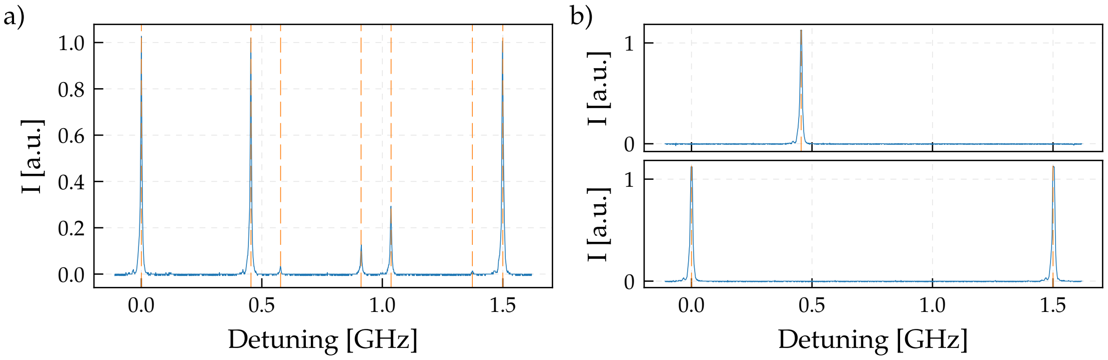

Figure 3.22: Frequency spectrum of the 2D-MOT TA output. a) Frequency spectrum of the 2D-MOT TA with cooling and repumping frequencies coupled in, measured with a Fabry-Perot interferometer. Besides the two laser frequencies, the spectrum also shows intermodulation products due to carrier-density modulations in the gain medium. b) Frequency spectrum with only the cooling light (upper graph) and only the repumping light (lower graph) coupled into the TA. The frequency-axis has been calibrated with a free spectral range of 1.5 GHz.

pass diffraction efficiencies of about 75 % were achieved. The output beams from all four AOM paths have comparable beam diameters, which leads to good combined coupling efficiencies using a 11 mm coupling lens. The AOM frequencies were initially set to values from a previous experiment cooling potassium atoms. For the 2D-MOT, the cooler AOM was set to a frequency of -119 MHz and the repumper AOM to 107 MHz. For the 3D-MOT, both cooler and repumper AOMs were set to a frequency of ± 111 MHz.

In a next step, the combined repumping and cooling light for the 2D-MOT was coupled into a single mode fiber and injected into the second tapered amplifier. To analyze if a simultaneous amplification of two different frequencies is possible and produces stable results, a small part of the amplifier output was sampled and coupled into a Fabry-Perot interferometer (FPI) [40]. Figure 3.22 shows the obtained spectrum. Blanking one of the frequencies at a time allows the assignment of the peaks. Using a free spectral range (FSR) of 1.5 GHz for this FPI, the frequency axis can be calibrated. The cooling and repumping frequencies have a separation of 455.0 MHz, which is in agreement with the set AOM frequencies. The combined spectrum shows the occurrence of several further peaks with different amplitudes. These peaks are *intermodulation products* (IMP), which are created when the two input frequencies nonlinearly interact inside the gain medium[42]. The beat frequency of the input signals causes a modulation of the carrier density inside the semiconductor, and the resulting gain and refractive index fluctuations give rise to non-degenerate four-wave mixing (FWM). The input frequencies ω_1 and ω_2 with a difference $\delta = \omega_2 - \omega_1 > 0$ cause IMPs at $\omega_1 - n\delta$ and $\omega_2 + n\delta$, where $n > 0$ is the order. Hence, the peaks at 911.8 MHz and 1373.7 MHz are positive IMPs and correspond to twice and three times the frequency difference. Because the negative IMPs lie outside the shown FSR, the two peaks at 577.9 MHz and 1036.3 MHz are negative IMPs from the next FSR. This could be verified by changing one AOM frequency which shifted the positive IMPs to the right, whereas the negative IMPs were shifted to the left. While

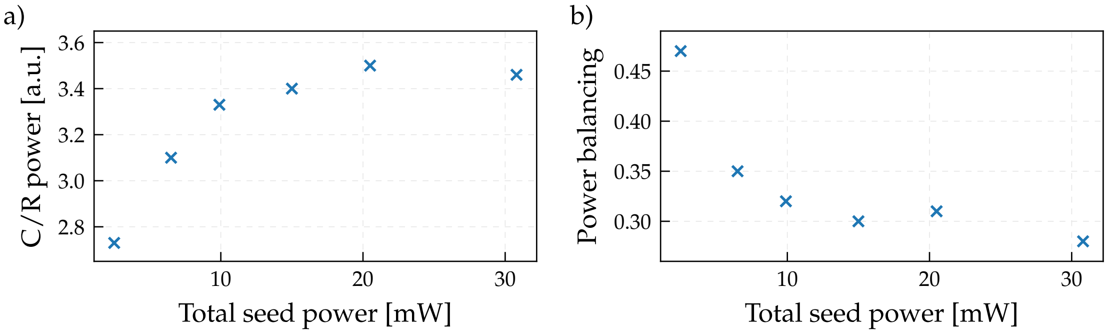

Figure 3.23: Power balancing of the 2D-MOT TA output. a) The power in the Cooling/Repumping frequency components increases for higher seed powers as expected (cf. Figure 3.17a). b) Ratio of cooler to repumper power required for balanced frequency components in the amplified beam. For higher total seed powers, an increasing amount of the repumper frequency has to be applied to balance the components.

the power in higher order IMPs is expected to decrease monotonously, the asymmetrical peak heights are likely to originate from a distortion of the gain modulation to a form which produces more negative-order sidebands.

Although the IMPs are too far away from the atomic resonances to interfere with the cooling and trapping cycles, the total output power of the amplifier is shared among these modes. It was observed that the relative power of the IMPs compared to the input frequencies increases with higher seed powers. Despite this power loss into the unwanted components, Fig. 3.23a confirms that the power of the cooler/repumper frequencies as a function of the seed power still follows the saturation behavior as analyzed in Fig. 3.17a. Therefore, a strong seeding is favorable as long as the unwanted components do not disturb the experiment.

While optimizing the amplifier output, it was observed that an equal balancing of both frequencies requires significantly different seed powers. In Fig. 3.23b, this effect was investigated with respect to the total seed power. At low powers, a ratio close to the expected value of 0.5 is measured. However, as the seed power is increased, the cooler increasingly dominates the gain, and more than three times as much repumping seed power is needed to balance the output. While this effect cannot be unambiguously explained, it could hint to a frequency-dependent gain profile of the tapered amplifier diode. The ratio could not be inverted by changing the amplifier current or the input power.

3.7 Optical Setup on the Science Table

As depicted in Fig. 3.21, the cooling and repumping frequencies for 2D- and 3D-MOT are combined and coupled into single-mode fibers which transport them to the science table. The optical setup for the 2D-MOT is shown in Fig. 3.24. The combined light is collimated with a $f = 12\,\mathrm{mm}$ lens to give a beam with a diameter of 2.2 mm. In a PBS cube, the horizontal and vertical directions are split, while the power balancing can be adjusted with a half-wave plate. From here on, the horizontal and vertical directions are built in a similar fashion. First, a Galilean telescope expands the beam to a diameter of 12 mm, before the light is split into the required counter-propagating beams for the 2D-MOT. Directly in front of the vacuum chambers, quarter-wave plates circularly polarize all four beams. To further raise the loading rate, a push beam blows the cold atoms through the differential pumping tube towards the 3D-MOT chamber. The push beam contains only the cooling frequency, and is brought to the science table by a separate fiber.

The optical setup for the 3D-MOT is shown in Fig. 3.25. The expanding beam from the fiber port is collimated with a $f = 80\,\mathrm{mm}$ lens to give a diameter of 15 mm. It is then split into the vertical and the two horizontal components via three polarizing beamsplitters. Each of the beams is again split into the two components which are sent through the glass cell counter-propagating. The crossing point coincides with the center of the quadrupole coils, where the cold cloud of atoms should form. Right in front of the glass cell, the linearly polarized light is circularized using quarter-wave plates.

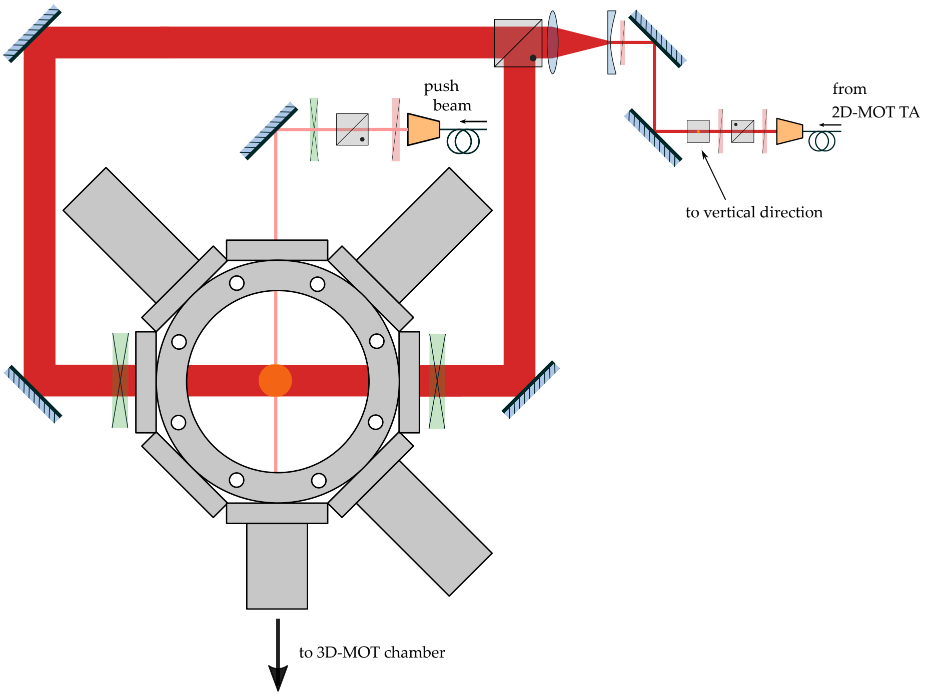

Figure 3.24: Optical setup for the 2D MOT. The combined cooling and repumping light for the 2D-MOT is split into a horizontal and vertical part, after which both parts are expanded in Galilean telescopes and sent through the MOT chamber. The push beam comes from a separate fiber and is positioned at the viewport opposite to the differential pumping stage. Vertical direction not shown for clarity.

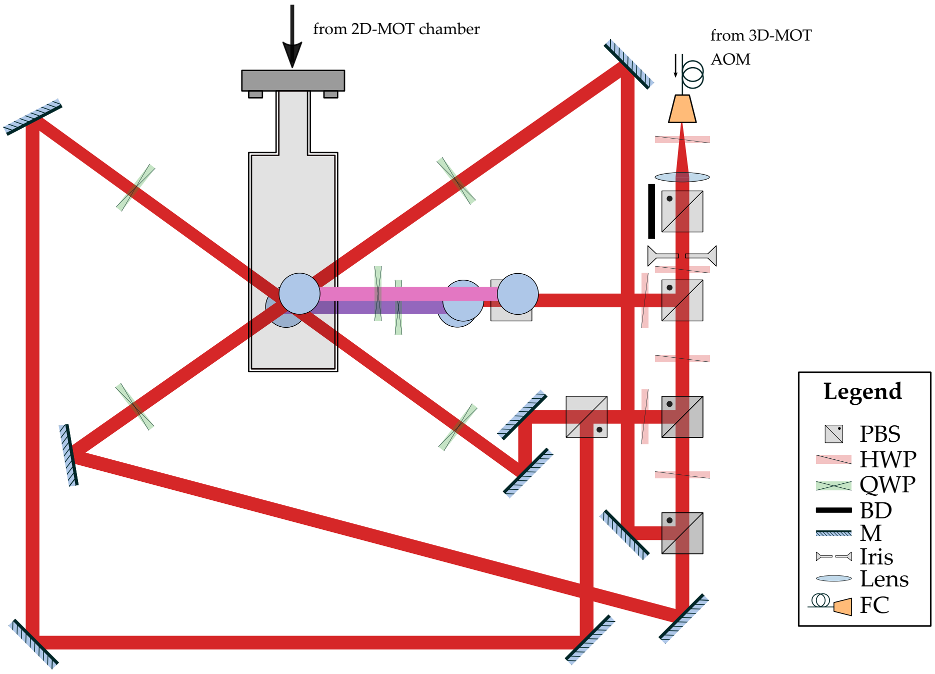

Figure 3.25: Optical setup for the 3D MOT. The six trapping beams are split via half-wave plate/PBS combinations and overlapped in the glass cell at the center of the magnet coils.

4 Towards the observation of the ^{39}K 3D-MOT

From a previous experiment, there was still a laser system set up for the cooling of ^{87}Rb atoms. The different cooling and repumping frequencies for both MOTs were coupled into single-mode fibers, and could be used to align the MOT optics. The difficulty of determining the right detunings and simultaneously adjusting the optics could therefore be avoided.

Initial adjustments with rubidium

The initial adjustments were performed with the rubidium light coupled into the 2D- and 3D-MOT fibers. As a first step, the 2D MOT was aligned. With the Rb oven heated up by a peltier element and a heating band, an elevated partial pressure of rubidium atoms inside the 2D MOT chamber was established. The horizontal and vertical beams were centered and overlapped with their counterparts via stencils on the viewports. The polarization of the MOT beams was set to right-handed for the horizontal beams and left-handed for the vertical beams using a Schäfter+Kirchhoff polarization analyzer. The laser power after the fiber coupler was measured to be about 130 mW of cooling light mixed with about 2 mW of repumping light. With a deactivated push beam, the MOT fluorescence inside the chamber was observed through the push beam viewport with a computer web camera. The trace of the trapping beams were clearly visible, indicating correct frequencies. As a next step, the orientation of the magnetic field was set. When the field orientation is correct with respect to the polarization of the MOT beams, the fluorescence is expected to concentrate as atoms are pushed to the trap center. This effect was visible for only one polarity, indicating the correct orientation.

The observation of the 2D-MOT is now mainly dependent on the correct balancing of the individual beam intensities. As this parameter is critical, the intensities were adjusted to be equal using a power meter beforehand. Now, the balancings must be walked against each other under close observation of the camera window. As soon as a tiny accumulation of fluorescing atoms can be observed, the signal is maximized with careful adjustments. It can be ensured that the signal indeed originates from cooled atoms instead of a reflection or persistent artifacts by slightly adjusting the balancing and watching the cloud move or change its shape. Figure 4.1 shows the 2D-MOT chamber as seen from the push beam viewport. The bright traces originate from background rubidium atoms that fluoresce in the horizontal and vertical beams. In the left picture, the repumping light was blocked, leading to no formation

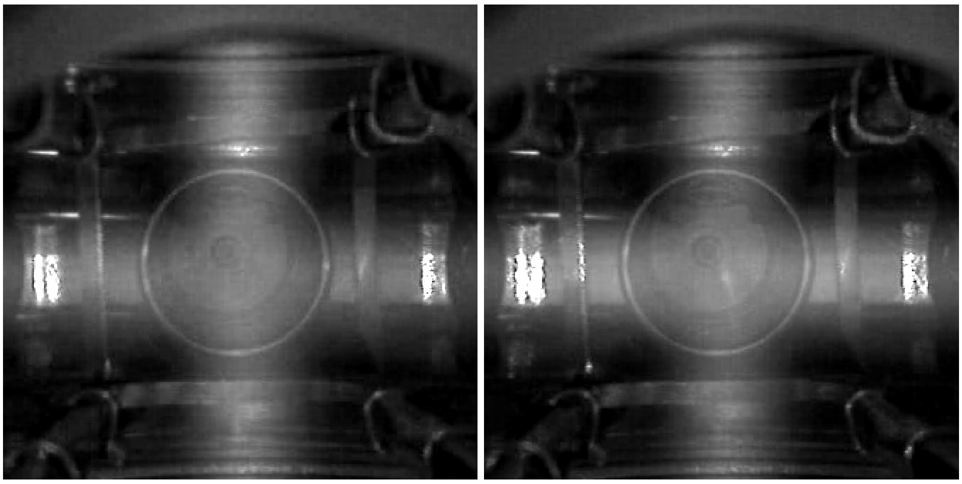

Figure 4.1: The Rb 2D-MOT. Left: 2D-MOT chamber with repumping frequency blocked. The thick traces originate from atoms fluorescing in the horizontal/vertical beams. Without the repumper, no MOT can be seen. Right: One of the first signals of the Rb 2D-MOT. Images as seen through the push beam viewport, observed with a webcam.

of a MOT. When the repumping frequency is added, a tiny cloud of rubidium atoms is formed (right picture). Behind the atom cloud, the differential pumping tube can be seen.

The next step was to build up the 3D-MOT optics and overlap the six laser beams with the crossing point in the center of the magnet coils. Because the 3D-MOT requires only about 50 mW in total and has a different detuning than the 2D-MOT cooler, it comes from a different AOM path. The repumping light is not mixed into the fiber, but an irradiation of the MOT from one side is sufficient. For the Rb test setup, a fiber coupler was directly aimed at the trap center and the collimation lens was positioned to obtain a diverging beam that irradiates the complete overlap region of the trap beams. The power of the individual beams was adjusted to be equal with a power meter directly in front of the glass cell. It was found that the formation of the MOT critically depends on the overlapping of the six beams. A double-check of the alignment helped to observe a tiny cloud. Because the loading times are very long, each adjustment must be done slowly and carefully. As soon as the position of the cloud has been determined, a CCD camera can be used to observe the 3D-MOT in detail and quantify the fluorescence signal. When first optimizations have been carried out, a value for the loading rate of the trap can be obtained by periodically emptying the trap. With the help of this signal, the parameters of 2D- and 3D-MOT can be optimized iteratively to obtain a maximum loading rate. Figure 4.2 shows the cloud of Rb atoms in the glass cell. The left picture was obtained with a conventional computer webcam, while the right one was captured with a Guppy CCD camera and converted into a false-color image.

Switch to potassium atoms

As soon as the laser system for potassium had been finished, the single-mode fibers for 2D- and 3D-MOT were removed from the fiber couplers in the rubidium laser systems and

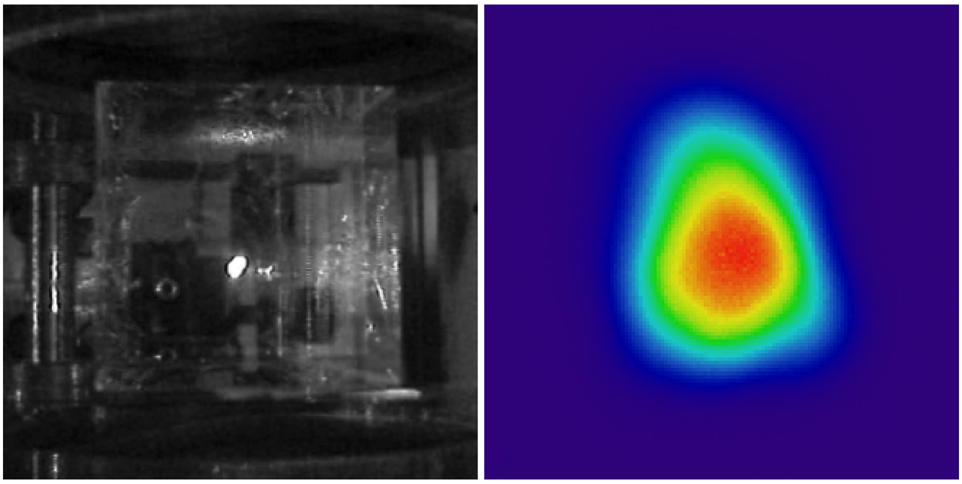

Figure 4.2: The Rb 3D-MOT. Left: Rb 3D-MOT in the glass cell after slight optimizations, observed using a webcam. Right: False-color image of the Rb 3D-MOT, captured with a Guppy CCD camera from the top of the cell.

attached to the ^{39}K laser system. After coupling the light and heating the potassium oven, fluorescence from the beams in the 2D-MOT chamber could be observed. The optimization of the rubidium 3D-MOT resulted in unbalanced counter-propagating beams, which was corrected by a manual balancing with the power meter. With the set AOM frequencies of $\pm 111\,\mathrm{MHz}$, no 3D-MOT could be observed. However, by unlocking the laser and slowly tuning it free-running, a very weak 3D-MOT was obtained by chance. From there, the AOM frequencies were adjusted to shift the required locking point towards the slope of the crossover error signal. Once the laser was lockable, the power balancing and the AOM frequencies for the 2D-MOT could be optimized. To obtain a sizable loading rate, the push beam still has to be coupled and aligned.

5 Conclusion and Outlook

This thesis describes the construction of a laser system for laser cooling of ^{39}K atoms. The light required for driving the D1- and D2-transitions in ^{39}K is generated by two ECDLs, which are locked to the atomic resonances in a custom Doppler-free saturated absorption spectroscopy setup. To supply the 2D- and 3D-MOT with sufficient amounts of light, the lasers are amplified in two home-built tapered amplifier modules, which have been set-up and aligned in the course of this thesis. Four double-pass AOM paths generate the cooling and repumping frequencies for both MOTs and allow for an individual adjustment of the detunings. After the trap optics were aligned with rubidium atoms, the observation of a ^{39}K 3D-MOT confirmed the correct operation of the laser system.

The next steps in the construction of the experiment aim towards Bose-Einstein condensation of the potassium atoms. To initiate an efficient evaporation, a gray molasses on the D1 transition is going to be employed. As the ECDL and the spectroscopy for the D1 gray molasses have already been set up, the third TA and two other AOM paths are going to be built and adjusted for the generation of the gray molasses light. When the magneto-optical traps are optimized for a sufficiently high loading rate ($\sim 1 \times 10^9\,\mathrm{s}^{-1}$), the gray molasses light is mixed with the 3D-MOT light. At this point, an experiment control needs to be established to shut down the magnetic field at the end of each loading cycle for a brief amount of time, in which a phase of pure optical molasses is done. By measuring atom number and temperature in the cloud, the gray molasses is optimized. In the following, the laser for the optical dipole trap is set up. For this, a Nd:YAG diode-pumped solid-state laser with an output power of 50 W at a wavelength of 1064 nm has already been purchased. As soon as the potassium cloud is sufficiently cold, the atoms are loaded into the dipole trap and evaporated to quantum degeneracy.

Once the condensate can be reproduced reliably, a vast amount of research possibilities await the experiment. A first research direction is the study of far-from-equilibrium quantum dynamics, which is especially interesting regarding the occurrence of non-thermal fixed points. Near these fixed points, dynamical systems exhibit scale-free behavior and are grouped in universality classes according to their critical exponent. Surprisingly, the dynamics of very different systems, like isolated quantum systems and the early Universe, may fall in the same universality class [43]. Hence, experiments with ultracold quantum gases could reveal new insights to processes at much larger energy scales [44]. Another possibility is the study of dynamics in lower-dimensional quantum gases. Using special shaped optical lattices, e.g.

tubular and pancake-shaped 1D- or 2D- Bose gases can be created. Apart from this, the ECDLs and TA chips can be used to drive the ^{41}K D1- and D2 transitions (cf. the ^{41}K level scheme in Fig. A.1). With the use of different AOMs, the laser system can also be adapted for cooling the bosonic ^{41}K isotope. Furthermore, the Rb oven and the existing laser system would enable the study of KRb bose-bose mixtures.

All in all, the stable and flexible setup combined with the versatile atomic species promises an interesting future for this experiment.

Bibliography

[1] T. W. Hänsch and A. L. Schawlow, *Cooling of gases by laser radiation*, Optics Communications **13**, 68–69 (1975).

[2] W. Ketterle, *When atoms behave as waves: Bose-Einstein condensation and the atom laser (nobel lecture)*, Reviews of Modern Physics **74**, 1131–1151 (2002).

[3] K. B. Davis, M.-O. Mewes, M. R. Andrews, N. J. van Druten, D. S. Durfee, D. M. Kurn, and W. Ketterle, *Bose-Einstein Condensation in a Gas of Sodium Atoms*, Physical Review Letters **75**, 3969–3973 (1995).

[4] M. R. Matthews, B. P. Anderson, P. C. Haljan, D. S. Hall, C. E. Wieman, and E. A. Cornell, *Vortices in a Bose-Einstein Condensate*, Physical Review Letters **83**, 2498–2501 (1999).

[5] D. Jaksch, C. Bruder, J. I. Cirac, C. W. Gardiner, and P. Zoller, *Cold bosonic atoms in optical lattices*, Physical Review Letters **81**, 3108–3111 (1998).

[6] M. Greiner, "Ultracold quantum gases in three-dimensional optical lattice potentials", PhD thesis (Munich University, 2003).

[7] M. Greiner, O. Mandel, T. Esslinger, T. W. Hänsch, and I. Bloch, *Quantum phase transition from a superfluid to a Mott insulator in a gas of ultracold atoms*, Nature **415**, 39–44 (2002).

[8] S. Inouye, M. R. Andrews, J. Stenger, H.-J. Miesner, D. M. Stamper-Kurn, and W. Ketterle, *Observation of Feshbach resonances in a Bose-Einstein condensate*, Nature **392**, 151–154 (1998).

[9] C. Derrico, M. Zaccanti, M. Fattori, G. Roati, M. Inguscio, G. Modugno, and A. Simoni, *Feshbach resonances in ultracold 39 K*, New Journal of Physics **9**, 223 (2007).

[10] M. Landini, S. Roy, L. Carcagní, D. Trypogeorgos, M. Fattori, M. Inguscio, and G. Modugno, *Sub-Doppler laser cooling of potassium atoms*, Physical Review A **84**, 043432 (2011).

[11] R. L. D. Campbell, R. P. Smith, N. Tammuz, S. Beattie, S. Moulder, and Z. Hadzibabic, *Efficient production of large 39 K Bose-Einstein condensates*, Physical Review A **82**, 063611 (2010).

[12] D. Nath, R. K. Easwaran, G. Rajalakshmi, and C. S. Unnikrishnan, *Quantum-interference-enhanced deep sub-Doppler cooling of 39K atoms in gray molasses*, Physical Review A **88**, 053407 (2013).

[13] G. Salomon, L. Fouché, P. Wang, A. Aspect, P. Bouyer, and T. Bourdel, *Gray-molasses cooling of 39K to a high phase-space density*, EPL (Europhysics Letters) **104**, 63002 (2013).

[14] G. Salomon, L. Fouché, S. Lepoutre, A. Aspect, and T. Bourdel, *All-optical cooling of 39K to Bose-Einstein condensation*, Physical Review A **90**, 1033405 (2014).

[15] M. Landini, S. Roy, G. Roati, A. Simoni, M. Inguscio, G. Modugno, and M. Fattori, *Direct evaporative cooling of 39 K atoms to Bose-Einstein condensation*, Physical Review A **86**, 033421 (2012).

[16] K. Dieckmann, R. Spreeuw, M. Weidemüller, and J. Walraven, *Two-dimensional magneto-optical trap as a source of slow atoms*, Physical Review A **58**, 3891–3895 (1998).

[17] J. V. Prodan, W. D. Phillips, and H. Metcalf, *Laser production of a very slow monoenergetic atomic beam*, Physical Review Letters **49**, 1149–1153 (1982).

[18] D. Wineland and H. Dehmelt, *Proposed* 10^{14} $\Delta\nu < \nu$ *Laser Fluorescence Spectroscopy on* Tl^{+} *Mono-Ion Oscillator*, Bulletin of the American Physical Society **20**, 637 (1975).

[19] W. D. Phillips and H. Metcalf, *Laser deceleration of an atomic beam*, Physical Review Letters **48**, 596–599 (1982).

[20] B. Phillips, *Laser cooling and trapping of neutral atoms*, Reviews of Modern Physics **70**, 199–237 (1998).

[21] S. Chu, L. Hollberg, J. E. Bjorkholm, A. Cable, and A. Ashkin, *Three-Dimensional Viscous Confinement and Cooling of Atoms by Resonance Radiation Pressure*, Physical Review Letters **55**, 48–51 (1985).

[22] M. H. Anderson, J. R. Ensher, M. R. Matthews, C. E. Wieman, and E. A. Cornell, *Observation of Bose-Einstein Condensation in a Dilute Atomic Vapor*, Science **269**, 198–202 (1995).

[23] H. J. Metcalf and P. Straten, *Laser Cooling and Trapping* (Springer, Heidelberg, 1999).

[24] C. J. Foot, *Atomic Physics* (Oxford University Press, 2005).

[25] C. Cohen-Tannoudji, *Manipulating Atoms with Photons (Nobel lecture)*, Reviews of Modern Physics **70**, 166–190 (1998).

[26] P. D. Lett, R. N. Watts, C. I. Westbrook, W. D. Phillips, P. L. Gould, and H. J. Metcalf, *Observation of atoms laser cooled below the doppler limit*, Physical Review Letters **61**, 169–172 (1988).

[27] J. Dalibard and C. Cohen-Tannoudji, *Laser cooling below the Doppler limit by polarization gradients: simple theoretical models*, Journal of the Optical Society of America B **6**, 2023–2045 (1989).

[28] M. Weidemüller, T. Esslinger, M. A. Ol'shanii, A. Hemmerich, and T. W. Hänsch, *A Novel Scheme for Efficient Cooling below the Photon Recoil Limit*, Europhysics Letters (EPL) **27**, 109–114 (1994).

[29] G. Grynberg and J. Y. Courtois, *Proposal for a Magneto-Optical Lattice for Trapping Atoms in Nearly-Dark States*, Europhysics Letters (EPL) **27**, 41–46 (1994).

[30] A. Aspect, E. Arimondo, and C. Cohen-Tannoudji, *Laser Cooling below the One-Photon Recoil Energy by Velocity-Selective Coherent Population Trapping*, Physical Review Letters **61**, 826–829 (1988).

[31] F. Sievers, N. Kretzschmar, D. R. Fernandes, D. Suchet, M. Rabinovic, S. Wu, C. V. Parker, L. Khaykovich, C. Salomon, and F. Chevy, *Simultaneous sub-Doppler laser cooling of fermionic Li 6 and K 40 on the D1 line: Theory and experiment*, Physical Review A **91**, 023426 (2015).

[32] A. Burchianti, G. Valtolina, J. A. Seman, E. Pace, M. De Pas, M. Inguscio, M. Zaccanti, and G. Roati, *Efficient all-optical production of large Li 6 quantum gases using D1 gray-molasses cooling*, Physical Review A **90**, 043408 (2014).

[33] A. T. Grier, I. Ferrier-Barbut, B. S. Rem, M. Delehaye, L. Khaykovich, F. Chevy, and C. Salomon, *Λ-enhanced sub-Doppler cooling of lithium atoms in D1 gray molasses*, Physical Review A **87**, 063411 (2013).

[34] I. Stroescu, “On a cold beam of potassium atoms”, MA thesis (Heidelberg University, 2010).

[35] T. G. Tiecke, “Feshbach resonances in ultracold mixtures of the fermionic quantum gases 6li and 40k”, PhD thesis (University of Amsterdam, 2009).

[36] T. Heine and R. Heidemann, “Tunable Diode Laser System With External Resonator”, U.S. pat. 7970024 (2011).

[37] C. E. Wieman and L. Hollberg, *Using diode lasers for atomic physics*, Review of Scientific Instruments **62**, 1–20 (1991).

[38] L. Ricci, M. Weidemüller, T. Esslinger, A. Hemmerich, C. Zimmermann, V. Vuletic, W. König, and T. W. Hänsch, *A compact grating-stabilized diode laser system for atomic physics*, Optics Communications **117**, 541–549 (1995).

[39] F. Nicolai, “Design and construction of a fiber-coupled tapered amplifier system”, MA thesis (Heidelberg University, 2017).

[40] B. E. A. Saleh and M. C. Teich, *Fundamentals of Photonics* (John Wiley & Sons, 2003).

[41] E. A. Donley, T. P. Heavner, F. Levi, M. O. Tataw, and S. R. Jefferts, *Double-pass acousto-optic modulator system*, Review of Scientific Instruments **76**, 063112 (2005).

[42] T. E. Darcie, R. M. Jopson, and R. W. Tkach, *Intermodulation Distortion in Optical Amplifiers from Carrier-Density Modulation*, Electronics Letters **23**, 1392–1394 (1987).

[43] J. Schmiedmayer and J. Berges, *Cold Atom Cosmology*, Science **341**, 1188–1189 (2013).

[44] J. Berges, K. Boguslavski, S. Schlichting, and R. Venugopalan, *Universality Far from Equilibrium : From Superfluid Bose Gases to Heavy-Ion Collisions*, Physical Review Letters **114**, 061601 (2015).

A Appendix

A.1 Potassium Term Scheme

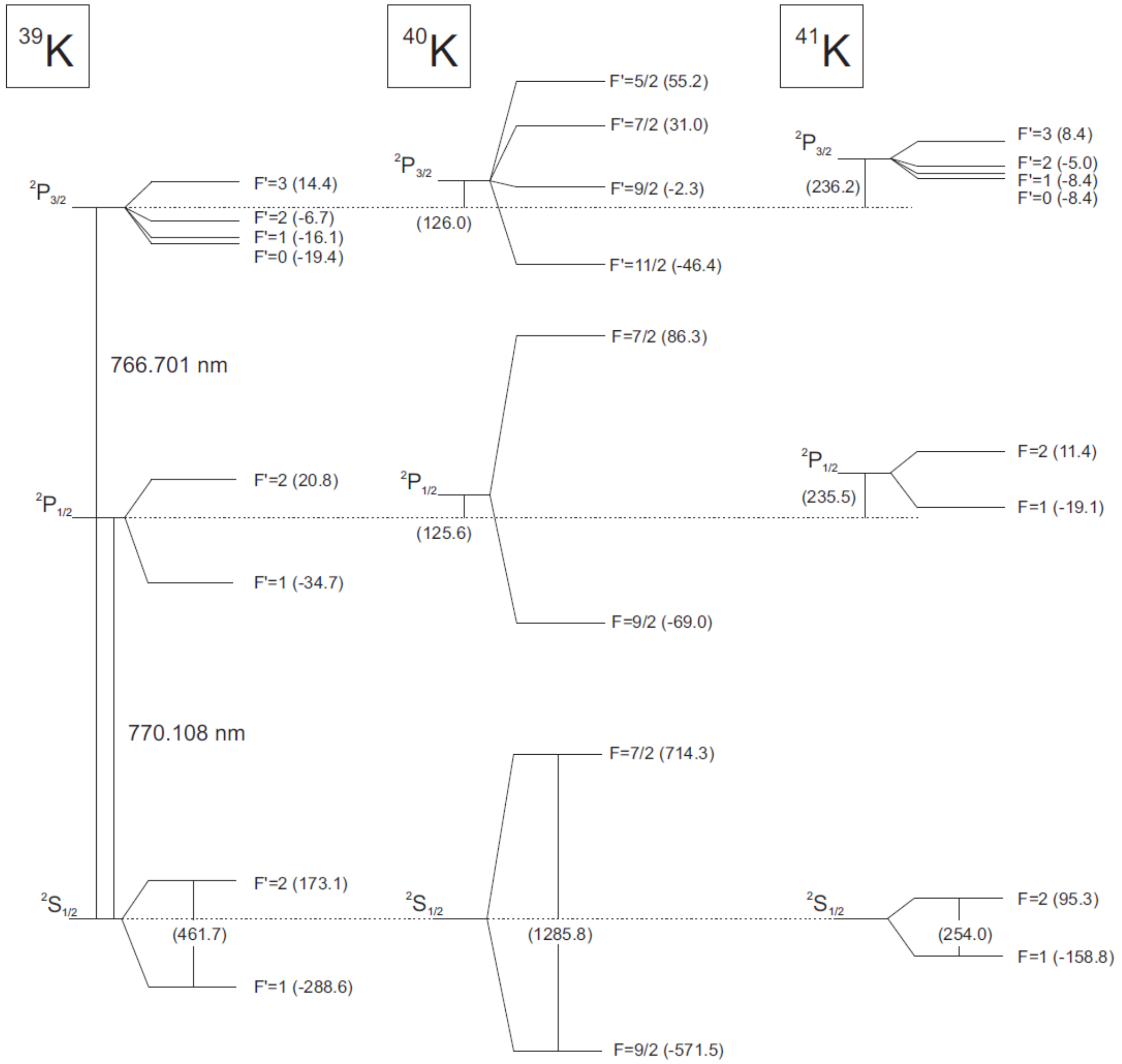

Figure A.1: Potassium term scheme. Term scheme for the three potassium isotopes ^{39}K, ^{40}K and ^{41}K showing the D1- and D2- transitions. From [35].

A.2 Technical Drawings

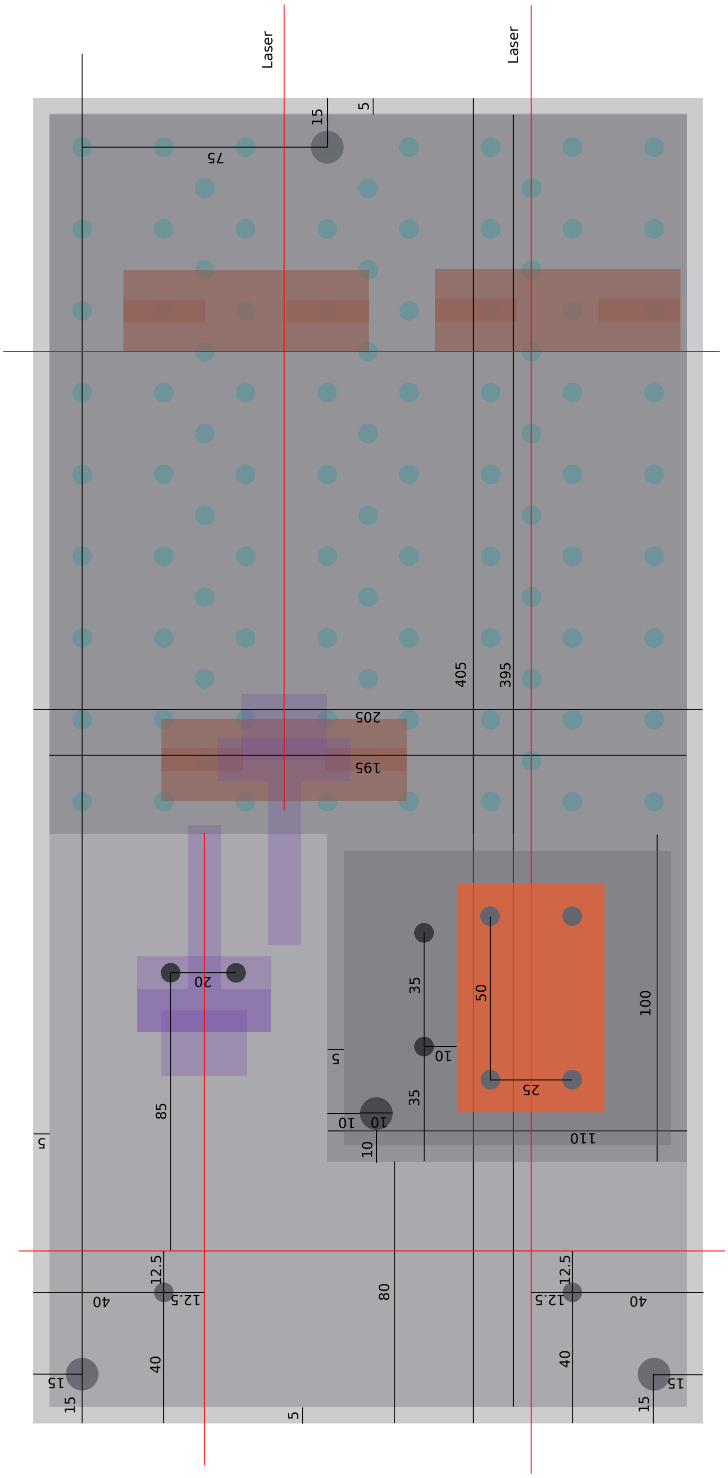

Figure A.2: TA Baseplate. Technical drawing of the aluminium block for the tapered amplifier module. The thin red lines mark the path of the laser beam.

B Acknowledgements

Zunächst möchte ich mich bei Markus Oberthaler für die Aufnahme in seine Gruppe und die Möglichkeit, beim Aufbau dieses spannenden Experiments mitzuwirken, bedanken. Sein stetiger Optimismus und seine Faszination für die Physik sind wirklich ansteckend! Selim Jochim danke ich für die Übernahme der Zweitkorrektur.

Besonderer Dank geht an das restliche BECK-Team, ohne das diese Arbeit nicht möglich gewesen wäre: Helmut hat mir immer wieder all meine Fragen beantwortet, und war stets mit dem entscheidenen Tipp zur Stelle. Danke auch für deinen Optimismus und deine unübertreffbare Gelassenheit, und für die super Betreuung! Celia, Maurus und Marius danke ich für die tolle Zeit im Labor und einige unterhaltsame Stunden sowie für die zahlreichen Korrekturvorschläge.

Selbstverständlich hat auch das restliche Matterwave-Team mit seiner gelassenen und offenen Art dafür gesorgt, dass man sich sehr schnell sehr wohl fühlt. Die gemeinsamen Aktivitäten, insbesondere der Drachenbootcup, haben für eine wunderbare Arbeitsatmosphäre gesorgt. Dem BEC-Team, mit dem ich mein Büro teilen durfte, danke ich für viele witzige Momente und das coole Büroklima.

Den ganzen neuen Freunden, die ich im Studium dazugewonnen habe, möchte ich ebenfalls danken. Liam, Adriana, Thuky, Timo, Ding ding und die anderen, danke für die zahlreichen lustigen und entspannenden Stunden, durch die der Stress des Studiums sehr gut ertragbar wurde!

An dieser Stelle möchte ich auch noch meinem Physiklehrer aus der Oberstufe, Alfred Simon, danken. Durch seine begeisternde Art, physikalische Fragestellungen den Schülern nahe zu bringen, hat er in mir erst die Faszination für die Physik geweckt. Ohne ihn würde ich jetzt vermutlich meine Bachelorarbeit in Informatik schreiben, und ich bin sehr froh, dass es nicht soweit gekommen ist.

Besonderer Dank gilt neben meiner Familie auch meiner Freundin Nina. Ohne dich wäre der ganze Stress nur halb so lohnenswert. Danke für deine unermüdliche Fürsorge und die super Zeit bisher. Ich bin froh, dass es dich gibt!

Erklärung

Ich versichere, dass ich diese Arbeit selbstständig verfasst und keine anderen als die angegebenen Quellen und Hilfsmittel benutzt habe.

Heidelberg, den 21. August 2017,